Cellular/Molecular

Different $Ca_V1.3$ Channel Isoforms Control Distinct Components of the Synaptic Vesicle Cycle in Auditory Inner Hair Cells

Philippe F.Y. Vincent,[1] Yohan Bouleau,[1] Gilles Charpentier,[1] Alice Emptoz,[2] Saaid Safieddine,[2] Christine Petit,[2,3] and Didier Dulon[1]

[1]Université de Bordeaux, Institut des Neurosciences de Bordeaux, Equipe Neurophysiologie de la Synapse Auditive, Inserm, Unité Mixte de Recherche en Santé 1120, Centre Hospitalier Universitaire Hôpital Pellegrin, 33076 Bordeaux, France, [2]Institut Pasteur et Université Pierre et Marie Curie, Unité de Génétique et Physiologie de l'Audition, Inserm, Unité Mixte de Recherche en Santé 1120, 75015 Paris, France, and [3]Collège de France, 75005 Paris, France

The mechanisms orchestrating transient and sustained exocytosis in auditory inner hair cells (IHCs) remain largely unknown. These exocytotic responses are believed to mobilize sequentially a readily releasable pool of vesicles (RRP) underneath the synaptic ribbons and a slowly releasable pool of vesicles (SRP) at farther distance from them. They are both governed by $Ca_v1.3$ channels and require otoferlin as Ca^{2+} sensor, but whether they use the same $Ca_v1.3$ isoforms is still unknown. Using whole-cell patch-clamp recordings in posthearing mice, we show that only a proportion (~25%) of the total Ca^{2+} current in IHCs displaying fast inactivation and resistance to 20 μM nifedipine, a L-type Ca^{2+} channel blocker, is sufficient to trigger RRP but not SRP exocytosis. This Ca^{2+} current is likely conducted by short C-terminal isoforms of $Ca_v1.3$ channels, notably $Ca_v1.3_{42A}$ and $Ca_v1.3_{43S}$, because their mRNA is highly expressed in wild-type IHCs but poorly expressed in *Otof*$^{-/-}$ IHCs, the latter having Ca^{2+} currents with considerably reduced inactivation. Nifedipine-resistant RRP exocytosis was poorly affected by 5 mM intracellular EGTA, suggesting that the $Ca_v1.3$ short isoforms are closely associated with the release site at the synaptic ribbons. Conversely, our results suggest that $Ca_v1.3$ long isoforms, which carry ~75% of the total IHC Ca^{2+} current with slow inactivation and confer high sensitivity to nifedipine and to internal EGTA, are essentially involved in recruiting SRP vesicles. Intracellular Ca^{2+} imaging showed that $Ca_v1.3$ long isoforms support a deep intracellular diffusion of Ca^{2+}.

Key words: auditory; calcium channels; hair cells; synaptic exocytosis

Significance Statement

Auditory inner hair cells (IHCs) encode sounds into nerve impulses through fast and indefatigable Ca^{2+}-dependent exocytosis at their ribbon synapses. We show that this synaptic process involves long and short C-terminal isoforms of the $Ca_v1.3$ Ca^{2+} channel that differ in the kinetics of their Ca^{2+}-dependent inactivation and their relative sensitivity to the L-type Ca^{2+} channel blocker nifedipine. The short C-terminal isoforms, having fast inactivation and low sensitivity to nifedipine, mainly control the fast fusion of the readily releasable pool (RRP); that is, they encode the phasic exocytotic component. The long isoforms, with slow inactivation and great sensitivity to nifedipine, mainly regulate the vesicular replenishment of the RRP; that is, the sustained or tonic exocytosis.

Introduction

The ribbon synapses of auditory inner hair cells (IHCs) encode critical information on sound timing and intensity into a specific afferent discharge rate that shows fast onset, rapid adaptation, and a sustained pattern as long as the sound signal is maintained (Kiang, 1965). To perform this neural encoding faithfully, IHCs use two key elements at their ribbon active zones: $Ca_v1.3$ Ca^{2+} channels, which provide a fast and a focalized voltage-gated Ca^{2+} entry (Brandt et al., 2005; Frank et al., 2009; Vincent et al., 2014),

Received July 27, 2016; revised Jan. 27, 2017; accepted Feb. 1, 2017.

Author contributions: P.F.Y.V. and D.D. designed research; P.F.Y.V., Y.B., G.C., A.E., S.S., and D.D. performed research; P.F.Y.V., Y.B., G.C., A.E., S.S., C.P., and D.D. analyzed data; P.F.Y.V. and D.D. wrote the paper.

This work was supported by the Fondation Agir Pour l'Audition (2015-APA Research Grant "Deciphering the role of otoferlin and Usher proteins at the auditory hair cell ribbon synapse" to D.D.). We thank the Bordeaux Imaging Center, a service unit of the CNRS-INSERM and Bordeaux University, member of the national infrastructure France BioImaging, where the confocal high-resolution immunomicroscopy of $Ca_v1.3$ channels and ribbons was done.

The authors declare no competing financial interests.

Correspondence should be addressed to Didier Dulon, Université de Bordeaux, Institut des Neurosciences de Bordeaux, Equipe Neurophysiologie de la Synapse Auditive, Inserm, Unité Mixte de Recherche en Santé 1120, Centre Hospitalier Universitaire Hôpital Pellegrin, 33076 Bordeaux, France. E-mail: didier.dulon@inserm.fr.

DOI:10.1523/JNEUROSCI.2374-16.2017

 0270-6474/17/372960-16$15.00/0

and otoferlin, a large, six-C2 domain protein that acts as a high-affinity Ca^{2+} sensor that has been proposed to control vesicle fusion (Roux et al., 2006; Beurg et al., 2010). Exocytosis at this synapse displays a fast component reflecting the fusion of a readily releasable pool of vesicles (RRP) tethered to the ribbon and a slowly releasable pool (SRP) corresponding to the recruitment of distant vesicles (Moser and Beutner, 2000; Spassova et al., 2004; Johnson et al., 2005). Both exocytotic components are Ca^{2+} dependent and require the putative Ca^{2+} sensor otoferlin (Roux et al., 2006; Pangrsic et al., 2010; Levic et al., 2011; Vincent et al., 2014), but whether they involve similar $Ca_v1.3$ Ca^{2+}-channels remains to be investigated.

In numerous tissues, the transcripts of $Ca_v1.3$ Ca^{2+} channels can undergo extensive alternative splicing resulting in protein isoforms, in particular in the C-terminal region underlying different gating properties (Bock et al., 2011; Huang et al., 2013). Notably, two $Ca_v1.3$ splice variants with early termination of the C terminus have been shown to yield to $Ca_v1.3_{42A}$ and $Ca_v1.3_{43S}$ isoforms. These short $Ca_V1.3$ isoforms Ca^{2+} channels are endowed with extremely fast inactivation and low sensitivity to dihydropyridine drugs (Huang et al., 2013). Interestingly, $Ca_v1.3_{42A}$ mRNA transcripts have been detected in the mouse organ of Corti (OC) (Singh et al., 2008). Moreover, $Ca_v1.3_{43S}$ mRNA transcripts have been found in the mouse IHCs (Scharinger et al., 2015), but their putative role in IHC exocytosis has not been investigated. In the present study, we used the different dihydropyridine sensitivity between $Ca_v1.3$ long and short isoforms to probe their specific role in IHC exocytosis. We also used the property of nifedipine of being switched instantaneously into an ineffective nitroso compound upon UV-flash illumination (Morad et al., 1983; Sanguinetti and Kass, 1984; Feldmeyer et al., 1995) to investigate the sequential role of long and short C-terminal isoforms of the $Ca_v1.3$ channels in RRP and SRP exocytosis. Furthermore, because $Ca_v1.3$ channels and otoferlin are thought to interact physically at the synapse (Ramakrishnan et al., 2009), the expression of these $Ca_v1.3$ isoforms was also investigated in mouse IHCs lacking otoferlin.

Materials and Methods

Tissue preparation

Experiments were performed in accordance with the guidelines of the Animal Care Committee of the European Communities Council Directive (86/609/EEC) and the ethics committee of the University of Bordeaux. All mice (C57BL6 of either sex) were anesthetized by intraperitoneal injection of a xylazine (6 mg/ml) and ketamine (80 mg/ml) mixture (Sigma-Aldrich) diluted in physiological saline. Cochlear organs were dissected from littermate controls ($Otof^{+/+}$, $Otof^{+/-}$), here termed wild-type (WT), or from knock-out otoferlin C57BL/6 mice ($Otof^{-/-}$) as described previously (Vincent et al., 2014).

Electrophysiological recordings from IHCs were obtained in whole-mount OCs from mice at postnatal days 14–18 (P14–P18); that is, after the onset of hearing. The OC was freshly dissected under binocular magnification in an extracellular solution maintained at 4°C containing the following (in mM): NaCl 135, KCl 5.8, $CaCl_2$ 1.3, $MgCl_2$ 0.9, NaH_2PO_4 0.7, glucose 5.6, Na pyruvate 2, and HEPES 10, pH 7.4, 305 mOsm. The tectorial membrane was carefully removed. The OC was placed in a recording chamber and the IHCs were observed with a 60× water-immersion objective [CFI Fluor 60× W near infrared (NIR), working distance (WD) = 2.0 mm, numerical aperture (NA) = 1; Nikon] attached to an upright Nikon FN1 microscope. The extracellular solution was complemented with 0.25 μM Apamin (Latoxan) and 0.2 μM XE-991 (Tocris Bioscience) to block SK channels and KCNQ4 channels, respectively. The external Ca^{2+} concentration was increased from 1.3 to 5 mM to enhance the amplitude of Ca^{2+} currents. All experiments were performed at room temperature (22–24°C).

Whole-cell recording and capacitance measurement

All IHC recordings were performed in the 20–40% normalized distance from the apex, an area coding for frequencies ranging from 8 to 16 kHz, using an EPC10 amplifier controlled by Patchmaster pulse software (HEKA Elektronik). Patch pipettes were pulled with a micropipette Puller P-97 Flaming/Brown (Sutter Instruments) and fire-polished with a Microforge MF-830 (Narishige) to obtain a resistance range from 3–5 MΩ. Patch pipettes were filled with a cesium-based intracellular solution containing the following (in mM): CsCl 145, $MgCl_2$ 1, HEPES 5, EGTA 1, TEA 20, ATP 2, and GTP 0.3, pH 7.2, 300 mOsm. In a few experiments, the concentration of the slow Ca^{2+} chelator EGTA was increased to 5 mM.

Ramp stimulation. Cells were held at −80 mV and depolarized from −90 mV to +30 mV in 120 ms giving a slope of voltage change of 1 mV/ms. IV curves were fitted with a Boltzmann function from −70 to −10 mV to obtain the half-maximal voltage activation potential ($V_{1/2}$) and the slope k using the following equation:

$$I_{(V)} = I_{max}/(1 + e^{(V_{1/2}-V)/k})$$

Where I_{max} is the maximal current.

Real-time capacitance measurement. Membrane capacitance (C_m) measurements were performed using Patchmaster Lock-in amplifier software (HEKA) as described previously (Vincent et al., 2014). A recruitment voltage depolarizing protocol was used to probe both the vesicular RRP fusion and the recruitment of SRP vesicles at the active zones. This protocol consisted in a train of 100 ms repetitive voltage steps from −80 mV to −10 mV, each stimulation being separated by a 100 ms interval.

Nifedipine experiments

Flash photoinactivation of nifedipine. We used the property of nifedipine to be inactivated by UV light (Morad et al., 1983; Feldmeyer et al., 1995) to restore the Ca^{2+} current instantaneously in IHCs. Ca^{2+} currents of IHCs were blocked by adding 20 μM the dihydropyridine blocker nifedipine to the external solution (Sigma-Aldrich, catalog #N7634). To allow efficient diffusion and blocking of Ca^{2+} currents by nifedipine, the OCs were always incubated for 5–10 min with the drug before starting to patch. Photoinactivation of nifedipine was achieved by applying brief UV flashes from a UV LED light source (Mic-LED 365, 128 mW; Prizmatix). The UV LED device was connected directly to the epi-illumination port at the rear of the upright Nikon FN1 microscope and illumination was focalized through the 60× objective (CFI Fluor 60X W NIR, WD = 2.0 mm, NA = 1; Nikon) and TTL triggered by the Patchmaster software.

Dose–response curve experiment. We incubated the OCs with different concentrations of extracellular nifedipine from 1 nM to 100 μM. All recordings started after 10–15 min of incubation with nifedipine. Ca^{2+} current amplitudes obtained at various nifedipine concentration were expressed as a percentage of the Ca^{2+} current recorded in the control bath (i.e., without nifedipine). Nifedipine was diluted in dimethyl sulfoxide (DMSO; Sigma-Aldrich, catalog #D8418). The final concentration of DMSO in the recording bath was always <1%. To be sure that DMSO did not affect the Ca^{2+} current, we performed recordings in the presence of 1% DMSO in the extracellular solution. Ca^{2+} current was similar with and without DMSO (data not shown). Data points were fitted with a sigmoidal Hill function as the following:

$$y = A_1 + (A_2 - A_1)\,x^n/(K^n - x^n)$$

where A_1 and A_2 are the minimum and the maximum Ca^{2+} current, respectively; x is the Ca^{2+} current at a given concentration of nifedipine; K is the Michaelis constant (i.e., IC_{50}), and n is the cooperative site.

Ca^{2+} imaging

Calcium imaging was performed from P14–P17 IHCs expressing the genetically encoded fast Ca^{2+} indicator GCamP6f (Chen et al., 2013). These IHCs were obtained by injecting the adeno-associated virus AAV2/8 containing the encoding sequence of GCamP6f through the round window of the cochlea of mice at age P3 *in vivo*. Whole mounts of the apical region of the OCs were dissected and mounted in the recording chamber as described above.

Image acquisition. As described by Vincent et al. (2014), changes in $[Ca^{2+}]_i$ were measured continuously with a C2 confocal system and

NIS-element imaging software (Nikon) coupled to the FN1 microscope. The dye was excited with a 488 nm solid-state laser (85-BCD-010-706; Melles Griot) and 500–530 nm emission recorded at 18 images/s.

Image analysis. Fluorescence emission was measured with ImageJ software by drawing a region of interest of 3.7 μm^2 (8 × 8 pixels) at the synaptic zones below the nucleus, at the region above the nucleus, and below the cuticular plate region (apical region). Emission fluorescent signals were analyzed and normalized by the ratio F/F_{min} ratio, where F_{min} was the minimum fluorescence found before starting stimulation.

Immunohistofluorescence

Preparation of tissues. The ramps of the cochlear apparatus of P14–P16 *Otof*$^{+/-}$ and *Otof*$^{-/-}$ mice were dissected and prepared as described previously by Vincent et al. (2014). Briefly, they were rapidly perfused with 100% methanol at −20°C for 30 min and washed with cold PBS. The inner ear was then incubated for 2 h in PBS solution containing 10% EDTA. The OC was then dissected and the tectorial membrane removed. Tissue was first incubated with PBS containing 30% normal horse serum for 1 h at room temperature. Synaptic ribbons, $Ca_v1.3$ channels, or vesicular transporter 3 (VGLUT3) and otoferlin were simultaneously labeled with anti-CtBP2 (goat polyclonal; Santa Cruz Biotechnology, catalog #SC-5966), anti $Ca_v1.3$ (rabbit polyclonal, Alomone Labs, catalog #ACC-005), or anti-VGLUT3 (rabbit polyclonal; Synaptic Systems, catalog #135 203) and anti-otoferlin (mouse monoclonal; Abcam, catalog #ab53233) antibodies, respectively. Actin-F was also used to visualize hair cells (1:100, Phalloidin Fluoprobe 405; Interchim, catalog #FP-CA9870). Secondary antibodies were used at 1:500: first donkey anti-goat Fluoprobe 547H (Interchim, catalog #FP-SB2110) and donkey anti-mouse Fluoprobe 647 (Interchim, catalog #FP-SC4110) and then goat anti-rabbit Alexa Fluor 488 after a PBS rinse (Invitrogen, catalog #A-11008). The surface preparation of OCs (apical turns) was then mounted on Superfrost-Plus glass slides (Kindler) in a Prolong-Antifade medium (Invitrogen) and kept in the dark at −20°C until observation.

Image acquisition. Samples were analyzed using a confocal laser scanning microscope Leica SP8 with a 63× oil-immersion objective (NA = 1.4) and white light laser (470 to 670 nm) (Bordeaux Imaging Center). Phalloidin was imaged by using a diode laser at 405 nm also mounted on the microscope. Stack images were acquired with the same parameters as in our previous study (Vincent et al., 2014).

Western blot

The OCs from the apical cochlear turn of 11 (*Otof*$^{-/-}$) and 18 (*Otof*$^{+/+}$) mice (P12–P14) were microdissected and homogenized in a RIPA lysis and extraction buffer containing the following (in mM): Na-HEPES 25, EDTA 5, and DTT 1, along with 1% Triton X-100, 0.5% Na-deoxycholate, and 20% SDS, pH 7.2, containing a protease inhibitor mixture (Roche). The protein concentration was measured with a Bradford protein essay. For each genotype, equals amount of protein (~15 μg) were resolved on 8% SDS-PAGE and transferred onto a nitrocellulose membrane (Whatman Protran BA85). Membranes were incubated overnight at 4°C in the primary antibody solution against the target protein $Ca_v1.3$ (rabbit polyclonal antibody directed against the N-terminal region of the protein, amino acid residues 215–227, corresponding to the second extracellular loop, Alomone Labs, catalog #ACC-005; dilution 1/200) and anti-VGLUT3 (Synaptic Systems, catalog #135 203; dilution 1/500) as an internal reference. The Western blot membranes were then incubated in the HRP-conjugated secondary antibody solution (Bethyl Laboratories, catalog #A120–2018P) for 1 h at room temperature. For imaging and analysis, the blots were developed using ECL reagents (LI-COR, WesternSure Premium Chemiluminescent Substrate, catalog #926-95010) and read on a LI-COR C-Digit blot scanner. The Western blot images were analyzed using LI-COR Image Studio version 5.0 software. Western blots were repeated two times. To test for nonspecific staining, preabsorption controls were performed. Primary $Ca_v1.3$ antibodies, preincubated with the antigenic peptide [Peptide (C)EQLTKETEGGNHS corresponding to amino acid residues 215–227 of rat $Ca_V1.3$] did not lead to any significant labeling of the blot membrane (data not shown).

Table 1. Sense and antisense primers used

cDNA	Name of primer	Primer sequence (5′–3′)	Product size (bp)
Myosin VIIa	6375s	CACCTGATGACTGGAAAC	340
	6715as	ATCATCCATTTTGTATCCC	
$Ca_v1.3$ (α_{1D})			
Exons 42–46	5010s	AGATGACGAGCCAGAAGACTCC	618
	5637as	GCTGCCTGGGTACCTGTTGTA	
Exon 42	4664s	CAACCCTGTTTGCTTTGGTC	331
	4995as	TATAGCCCGTCGGATTTCTG	
Exon 42A	4946s	ATGCTTGAACGGATGCTTTAG	200
	5146as	CTTCCTTCCGGAGGAGTGC	
Exon 44	5010s	AGATGACGAGCCAGAAGACTCC	440
	5450as	CTAATGTAAGTCTCGTAATAGCGGGT	
Δ44	5010s	AGATGACGAGCCAGAAGACTCC	452
	5462as	CCTGACTCAGACCTTTTAATACTG	

s, Sense; as, antisense.

RT-PCR

Isolation and precipitation of total RNA. Apical turns of 4 OCs from P35 *Otof*$^{+/-}$ or P35 *Otof*$^{-/-}$ mice were freshly dissected and stored in separate low-DNA-binding tubes containing 15 μl of RNase inhibitor (Amresco, catalog #E633) maintained in dry ice. Total RNA was extracted from tissues using the RNAzol protocol (Molecular Research Center, catalog #RN 190).

RT. mRNA (0.5 μg) was reverse transcribed to cDNA by using oligodT primers and AffinityScript Multiple Temperature Reverse Transcriptase (Stratagene, catalog #600107). RT was performed at 37°C overnight.

PCR. Specific PCR amplification was performed by using 0.45 μg of cDNA and Herculase II Fusion DNA Polymerase (Stratagene, catalog #600677). Sense and antisense primers (Eurofins Genomics) are summarized in Table 1.

RT-PCR (pooled IHCs). Apical turns from P18 mice were placed in the same recording chamber as that used for patch-clamp recording. Using a large patch pipette ($R \leq 1.5$ MΩ), we collected 6–10 IHCs and broke the tip of the patch-pipette in a low-DNA-binding tube resting on dry ice and containing 15 μl of RNase inhibitor. RT-PCR from IHCs was performed as aforementioned for the whole OC.

Real-time semiquantitative PCR (Q-PCR)

We performed Q-PCR from 0.45 μg of cDNAs obtained from apical turns of OC as described above. PCR amplification was stopped at cycles 30, 31, 32, 33, 34, and 36 and analyzed by plotting fluorescence intensity. Data points were fitted using a sigmoidal function. Intensity was normalized to noise level. We used the cycle threshold parameter (Ct) to compare the amplification of each isoform. Ct was determined by tracing a line at the lowest intensity corresponding to the exponential phase of the sigmoidal curve (i.e., between the start of the signal increase and the start of the linear phase of the sigmoidal curve). The Ct parameter was the intersection point between this line and the sigmoidal curve.

All PCR products obtained from OCs and pooled IHCs were cloned and sequenced.

Statistical analysis

Electrophysiological results were analyzed with Patchmaster (HEKA Elektronik), OriginPRO 9.1 (OriginLab), and IgorPro 6.3 (Wavemetrics) software. Results are expressed as mean ± SEM. Statistical analyses were performed with Student's *t* test. The limit of significance was set at $p < 0.05$.

Results

Nifedipine-resistant, fast-inactivating, Ca^{2+} current

The addition of 20 μM nifedipine to the extracellular medium, a concentration well above the submicromolar range IC_{50} of full-length $Ca_V1.3$ channels (Huang et al., 2013) and the IC_{50} of 69 nM that we have determined in a dose–response curve (see Fig. 2*D*,*E*) reduced the Ca^{2+} current amplitude in IHCs from posthearing mice (P14–P18) by nearly 75% from a mean peak value of

−184 ± 19 pA in the absence of nifedipine (control condition, black, $n = 8$) to a mean value of −46 ± 5 pA at −10 mV (nifedipine, green, $n = 17$; $p < 0.05$; Fig. 1*A*). Note that, even at 100 μM nifedipine, nearly 25% of the Ca^{2+} current remained unblocked (Fig. 2*E*). A similar effect of nifedipine on Ca^{2+} current has been found in rat cardiomyocytes, in which the IC_{50} is ~100 nM and 20% of the Ca^{2+} current is resistant to nifedipine (Pignier and Potreau, 2000). This nifedipine-resistant current (Fig. 1*A*, inset) showed a similar voltage dependence compared with the total current in the control condition. Indeed, when fitting the IV curves from −70 mV to −10 mV with a sigmoidal Boltzmann function, there was no significant difference in the $V_{1/2}$ (−27.9 ± 0.9 mV and −26.9 ± 0.8 mV, nifedipine and control condition, respectively; $p = 0.45$) or k (5.9 ± 0.4 pA/mV and 5.7 ± 0.2 pA/mV, nifedipine and control condition, respectively; $p = 0.69$).

To determine the kinetics of the Ca^{2+} current reactivation when UV-inactivating nifedipine, IHCs were UV flashed 20 ms after the Ca^{2+} current onset evoked by a 100 ms step depolarization from −80 mV to −10 mV (Fig. 2*A*,*B*). UV-flash photolysis instantaneously inactivated nifedipine and unblocked Ca^{2+} channels, leading to an exponential increase of Ca^{2+} current with a mean time constant of 8.4 ± 0.7 ms (Figs. 1*A*,*D*, 2*A*–*C*). The reactivated Ca^{2+} current showed a nearly 2.5-fold increase in amplitude from its blocked state, rising from a peak value of −46 ± 5 pA in the presence of nifedipine to −108 ± 10 pA after the UV flash ($n = 10$; $p < 0.05$; Fig. 1*A*, purple trace). In our experimental conditions, IHCs were flashed in a nifedipine-containing extracelllular solution. We believe that the UV flash, which is condensed through the 60× objective of the microscope, only inactivated nifedipine within few tens of micrometers around the IHCs. The uncomplete recovery of the Ca^{2+} current after the flash can be explained by a rapid diffusion and block by residual active nifedipine.

Comparison of the voltage-dependent parameters of the Ca^{2+} current before and after UV flash photolysis of nifedipine showed no significant changes either in $V_{1/2}$ (−27.9 ± 0.9 mV and −28.5 ± 1.5 mV, respectively, $p = 0.73$) or in the Boltzmann slope (k: 5.9 ± 0.4 pA/mV and 6.3 ± 0.2 pA/mV, respectively; $p = 0.42$; Fig. 1*A*, inset). The maximum reactivated Ca^{2+} currents reached nearly 60% of control values in the absence of nifedipine.

Control condition Ca^{2+} currents evoked during a 100 ms voltage step from −80 mV to −10 mV displayed a partial fast inactivation, corresponding to a reduction of 17.6 ± 2.2% ($n = 7$) of initial current at the end of the pulse (Fig. 1*C*, first pulse). A similar fast-inactivating component of Ca^{2+} currents was described previously in rat IHCs (Grant and Fuchs, 2008), turtle hair cells (Schnee and Ricci, 2003), and frog hair cells (Cho et al., 2014). This fast inactivation of Ca^{2+} channels was essentially due to Ca^{2+}-dependent inactivation because it was largely reduced when Ba^{2+} ions replace Ca^{2+} ions as the charge carrier (Fig. 3), as described previously (Platzer et al., 2000; Michna et al., 2003). The inactivated current amplitude (obtained by subtracting the current at the first pulse from the second pulse) in the presence of Ca^{2+} was 39.8 ± 8.1 pA versus 6.7 ± 2.4 pA in the presence of Ba^{2+} (Fig. 3*C*; $p < 0.05$).

In the presence of nifedipine, Ca^{2+} currents showed a similar fast inactivation with an amplitude corresponding to 54.6 ± 3.7% ($n = 8$) of the initial current (Fig. 1*D*, first pulse). The kinetics and amplitude of the fast-inactivating component of the Ca^{2+} current in both control and nifedipine conditions were obtained by subtracting current values between two consecutive 100 ms pulses (pulse 1 − pulse 2) separated by 100 ms (Fig. 1*F*). The fast-inactivating components in control and nifedipine conditions had a maximum amplitude of 40 ± 8 pA ($n = 7$) and 20 ± 3 pA ($n = 8$), respectively ($p < 0.05$). They showed similar fast-inactivating kinetics with a time constant of 3.8 ± 1.3 ms and 4.6 ± 0.9 ms in control and nifedipine conditions, respectively ($p = 0.57$). The inactivation kinetics of the Ca^{2+} current that we measured here could even be faster at physiological temperature, as shown previously by Grant and Fuchs (2008). Indeed, the biophysical properties of the ion channels, as well as exocytosis and vesicular recruitment, are known to be facilitated at body temperature (Kushmerick et al., 2006, Nouvian, 2007). Interestingly, our results showed that the fast-inactivating component of Ca^{2+} currents in IHCs is only poorly affected by nifedipine.

The time course of recovery of the Ca^{2+} current from inactivation was determined by using a paired-pulse protocol (each pulse of 50 ms duration from −80 mV to −10 mV) with different interpulse durations (Fig. 3*D*,*E*). The relationship between the amplitude of the Ca^{2+} current at the second pulse (normalized to the first pulse) and the interpulse interval could be best fitted with a single exponential function with $\tau = 33.7 \pm 2.3$ ms ($n = 8$; Fig. 3*E*). The recovery of the fast-inactivating component of the Ca^{2+} current, obtained by normalizing the inactivation time constant of I_{Ca} at the second pulse to the one obtained at the first pulse, indicated a similar time constant with $\tau = 41.9 \pm 9.3$ ms ($n = 8$; Fig. 3*E*). It is interesting that the time course of recovery of the Ca^{2+} current determined in the present study is in the range of the recovery time constant of sound-evoked short-term adaptation of the auditory nerve discharge rate (40–60 ms, Westerman and Smith, 1984; Spassova et al., 2004; Cho et al., 2011) but somewhat faster than the time constant of RRP recovery from depletion measured in IHCs (~140 ms; Moser and Beutner, 2000). These results suggest that the fast inactivation of the Ca^{2+} current could contribute to the short-term adaptation of transmitter release at the auditory ribbon synapses.

Reduced fast inactivation of Ca^{2+} current in IHCs lacking otoferlin

Inactivation of Ca^{2+} current was investigated in IHCs from P14–P18 otoferlin-deficient mice ($Otof^{-/-}$). We recall that otoferlin is thought to be the major Ca^{2+} sensor for IHC exocytosis (Roux et al., 2006; Beurg et al., 2010). This multi-C2 protein is believed to interact with the $Ca_v1.3$ II–III loop (Ramakrishnan et al., 2009). As described previously (Roux et al., 2006), we found that $Otof^{-/-}$ IHCs displayed Ca^{2+} current peak amplitudes similar to WT (−164 ± 7 pA, $n = 9$ and −184 ± 19 pA, $n = 8$, respectively; $p = 0.33$; Fig. 1*B*). The sigmoidal Boltzmann fit of the IV curve did not display any significant differences either in $V_{1/2}$ (−27.0 ± 0.7 mV and −26.9 ± 0.8 mV, $Otof^{-/-}$ and WT, respectively; $p = 0.93$) or in the slope factor k (6.3 ± 0.3 pA/mV and 5.7 ± 0.2 pA/mV, $Otof^{-/-}$ and WT, respectively; $p = 0.1$; Fig. 1*B*, inset). However, Ca^{2+} currents of $Otof^{-/-}$ IHCs displayed a largely reduced fast-inactivating component (Fig. 1*E*,*G*). Indeed, a 100 ms paired-pulse voltage-step protocol (pulse 1 to pulse 2) indicated a large reduction of the fast-inactivating component in $Otof^{-/-}$ IHCs compared with WT (15.0 ± 2.2 pA and 40 ± 8 pA, respectively, $p < 0.05$; Fig. 1*E*,*G*). The residual inactivating component in $Otof^{-/-}$ IHCs had similar kinetics to WT (4.1 ± 0.9 ms and 3.8 ± 1.3 ms, respectively, $p = 0.85$; Fig. 1*E*,*G*). These results suggest a reduced expression of fast-inactivating Ca^{2+} channels in IHCs lacking otoferlin.

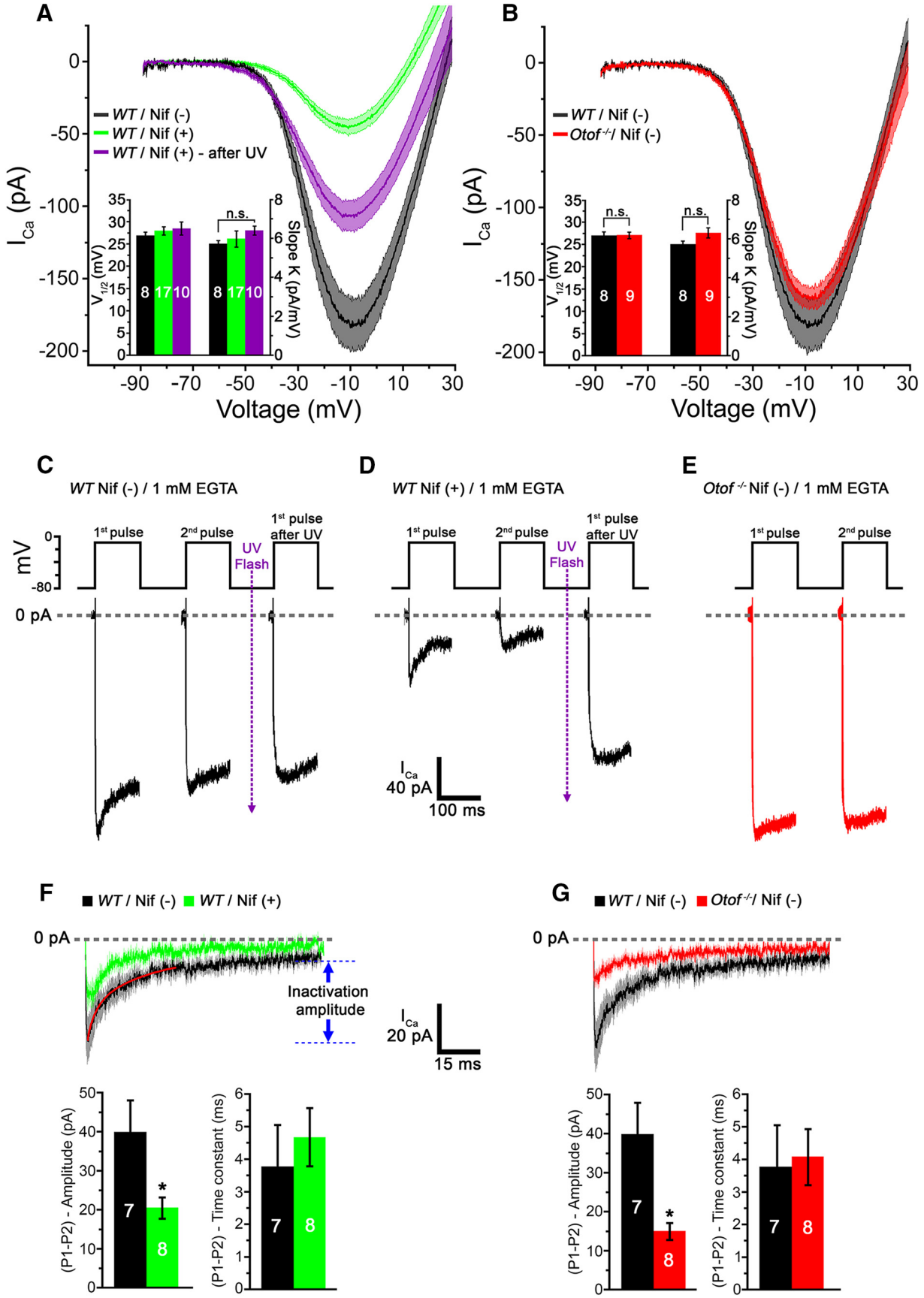

Figure 1. Nifedipine-resistant Ca^{2+} current in mature IHCs. ***A***, IV-ramp activation curve of Ca^{2+} currents from −90 mV to +30 mV in WT mice without nifedipine (control condition, black), with 20 μM nifedipine (green), and after the UV flash inactivation of nifedipine (purple). Inset shows the Boltzmann parameters ($V_{1/2}$ and k) obtained by fitting the IV curve from −70 mV to −10 mV with a Boltzmann sigmoidal function in the three different conditions. ***B***, Same protocol as in ***A*** for comparison between WT (black, same trace as in ***A***) and (*Figure legend continues.*)

Nifedipine-resistant Ca^{2+} currents trigger efficient fast RRP exocytosis

Surprisingly, although showing a large reduction in Ca^{2+} current in the presence of 20 μM nifedipine, WT P14-P18 IHCs displayed exocytotic amplitudes similar to control condition (20.15 ± 4.64 fF and 23.16 ± 2.53 fF, respectively, $p = 0.64$; Fig. 4*A*,*B*,*D*) when tested by 100 ms voltage steps from −80 to −10 mV. This indicated an apparent higher Ca^{2+} efficiency for RRP exocytosis in the presence of nifedipine (0.47 ± 0.08 fF/pA) compared with control IHCs in the absence of nifedipine (0.1 ± 0.02 fF/pA; $p < 0.001$). However, exocytosis in nifedipine-treated IHCs displayed larger paired-pulse depression (pulse 2/pulse 1 ratio) compared with controls (75 ± 5% and 32 ± 16%, respectively; $p < 0.05$; Fig. 4*A*,*D*,*E*). Increasing the concentration of intracellular EGTA from 1 to 5 mM in the presence of nifedipine only partially reduced the first exocytotic response to 13.5 ± 1.9 fF compared with 20.15 ± 4.64 fF, whereas the paired-pulse protocol showed similar depression to the nifedipine condition (59 ± 7.6% and 75 ± 5%, respectively; Fig. 4*C*,*D*; data in blue, $p = 0.08$).

Otof$^{-/-}$ IHCs showed a first exocytotic response reduced to 10.58 ± 2.34 fF ($p < 0.05$) and a larger 77% paired-pulse depression compared with WT IHCs (Fig. 4*D*,*E*, data in red).

We also compared the Ca^{2+} efficiency of exocytosis obtained with a 100 ms step depolarization from −80 mV to +5 mV, in 10 mV increments, in the presence of nifedipine (green) and after UV inactivation of nifedipine in the same WT IHCs (Fig. 4*F*,*G*, purple). Again, we found that exocytosis showed a higher Ca^{2+} efficiency in the presence of nifedipine compared with responses obtained after UV-unblocking Ca^{2+} channels (0.25 ± 0.01 fF/pA and 0.16 ± 0.01 fF/pA before and after UV flash, respectively, $p < 0.05$). These results can be explained by the fact that the Ca^{2+} current amplitude increased after the flash but not exocytosis. Because the efficiency is the ratio of $\Delta C_m/I_{Ca}$, the efficiency of exocytosis appears decreased after the UV flash. These results suggest that the IHC RRP release essentially depends on nifedipine-resistant Ca^{2+} currents.

Nifedipine severely impairs the sustained exocytotic component of the IHCs

A protocol of vesicle recruitment was tested by applying a train of 100 ms step depolarization from −80 mV to −10 mV with a 100 ms time interval in control and nifedipine-treated P14–P18 WT IHCs (Fig. 5*A*–*C*). To unblock Ca^{2+} channels, a UV flash was applied during the train of stimulation. In control WT IHCs, exocytosis first showed a slight depression after the second pulse and then a sustained linear increase that was not affected by the UV flash (Fig. 5*A*, *C*, black lines). In nifedipine-treated WT IHCs, exocytosis displayed a strong depression after the second pulse and the exocytotic response was restored only after a long latency ranging from 700 to 800 ms after the UV flash, although the Ca^{2+} current was instantaneously unblocked (Fig. 5*B*, *C*, green lines). In WT IHCs loaded with 5 mM intracellular EGTA in the presence of nifedipine, exocytosis showed a constant profound depression with no recovery after UV-unblocking Ca^{2+} current (Fig. 5*C*, blue lines). Provided that endocytosis is not enhanced in presence of nifedipine, a reasonable assumption because it is considered a slow, calcium-dependent process (Moser and Beutner, 2000; Cho et al., 2011), the present results suggest that the noninactivating nifedipine-sensitive Ca^{2+} currents regulate vesicular recruitment, possibly by allowing a deep intracellular diffusion of Ca^{2+} ions. We also observed similar sustained depression in *Otof*$^{-/-}$ IHCs (Fig. 5*D*, red lines), confirming the important role of otoferlin in the recruitment process (Pangrsic et al., 2010).

Imaging Ca^{2+} influx from nifedipine-resistant Ca^{2+} channels

Simultaneous Ca^{2+} imaging and whole-cell patch-clamp recordings were performed in P14–P18 WT IHCs expressing the genetically encoded fast Ca^{2+} indicator GCamP6f (Chen et al., 2013). These experiments were performed in the presence or in the absence of 20 μM nifedipine during a train of 100 ms step depolarization (Fig. 6). In control condition, the recruitment protocol led to a parallel increase in intracellular Ca^{2+} (Fig. 6*C*) and membrane capacitance (Fig. 6*A*). Intracellular Ca^{2+} instantaneously increased at the synaptic zones in two phases (Fig. 6*C*, black trace): a first phase (Ph1) that mirrored the fast-inactivating Ca^{2+} currents and a second slow component (Ph2) that corresponded to the sustained Ca^{2+} currents (Fig. 6*E*,*G*). A rise in intracellular Ca^{2+} was also recorded at extrasynaptic sites around and above the nucleus, but with a long delay of several hundred milliseconds and a much smaller amplitude compared with that of the synaptic zones (Fig. 6*C*,*G*,*H′*; orange trace). These results suggested a diffusion of Ca^{2+} from the synaptic zones, where Ca^{2+} channels are concentrated. Remarkably, the Ca^{2+} rise in this supranuclear region (Fig. 6*C*, orange trace) perfectly mirrored the sigmoidal increase in cumulative exocytosis during the train protocol (Fig. 6*A*). These results indicated that a deep intracellular diffusion of Ca^{2+} is associated with vesicular recruitment.

In nifedipine condition, at the synaptic zones, Ca^{2+} responses of Ph1 showed similar kinetics compared with the control condition (4.57 ± 0.9 ΔF/s ($n = 5$) and 4.75 ± 1.2 ΔF/s ($n = 5$), respectively; $p = 0.9$), but Ph2 was largely diminished (Fig. 6*D*,*F*,*H*). At the supranuclear zone of the cells, the Ca^{2+} responses were completely suppressed by nifedipine (Fig. 6*D*,*F*,*H′*). These results suggest that most of the fast-inactivating nifedipine-resistant Ca^{2+} channels are located at the basal synaptic active zones. UV photolysis of nifedipine instantaneously increased the Ca^{2+} current amplitude (Fig. 6*B*) and Ca^{2+} signals (Fig. 6*D*,*H*, Ph3). As also shown in Figure 5, *B* and *C*, the recovery of the exocytotic response displayed a long latency of several hundred milliseconds after the UV flash. Because nifedipine does not affect the intracellular exocytotic machinery directly, as indicated by the conserved first exocytotic jump (Fig. 4*B*,*D*), our results suggest that the delayed exocytotic recovery after unblocking Ca^{2+} channels is due to the time of intracellular Ca^{2+} diffusion and/or recruitment of vesicular stores located far away from the synaptic sites of release.

Remarkably, fast Ca^{2+} responses were also recorded at the subcuticular zone of WT IHCs in control condition during voltage step depolarization (Fig. 7*A*–*C*, light blue trace; $n = 7$). These Ca^{2+} responses peaked with no apparent delay with the Ca^{2+}

←

(*Figure legend continued.*) otoferlin-deficient mice (*Otof*$^{-/-}$, red). Inset shows the Boltzmann parameters ($V_{1/2}$ and k) for WT and *Otof*$^{-/-}$. ***C*–*E***, Example of Ca^{2+} current traces in response to a paired pulse of 100 ms depolarization from −80 mV (resting potential) to −10 mV. For control condition (***C***) and in the presence of 20 μM nifedipine (***D***), we applied a third 100 ms stimulation after the UV flash to test the UV unblocking of Ca^{2+} channels. ***F***, ***G***, Top traces show the inactivating Ca^{2+} currents (mean ± SEM) obtained after subtracting the second pulse response from the first. Histograms show the amplitudes and inactivation-time constants of the subtracted Ca^{2+} currents obtained in different conditions: control condition (black), with nifedipine (green), and in *Otof*$^{-/-}$ without nifedipine (red). Amplitude of inactivation was measured between the Ca^{2+} peak and the steady state of inactivation (blue dashed lines in ***F***). The fast-inactivating time constant was determined by fitting the current decrease with an exponential function (red line in ***F***). Error bars indicate SEM. Nif (−), condition without nifedipine; Nif (+), condition with 20 μM nifedipine. *$p < 0.05$ in ***A***, ***B***, ***F***, and ***G***. The number of cells is indicated for each condition in the histograms.

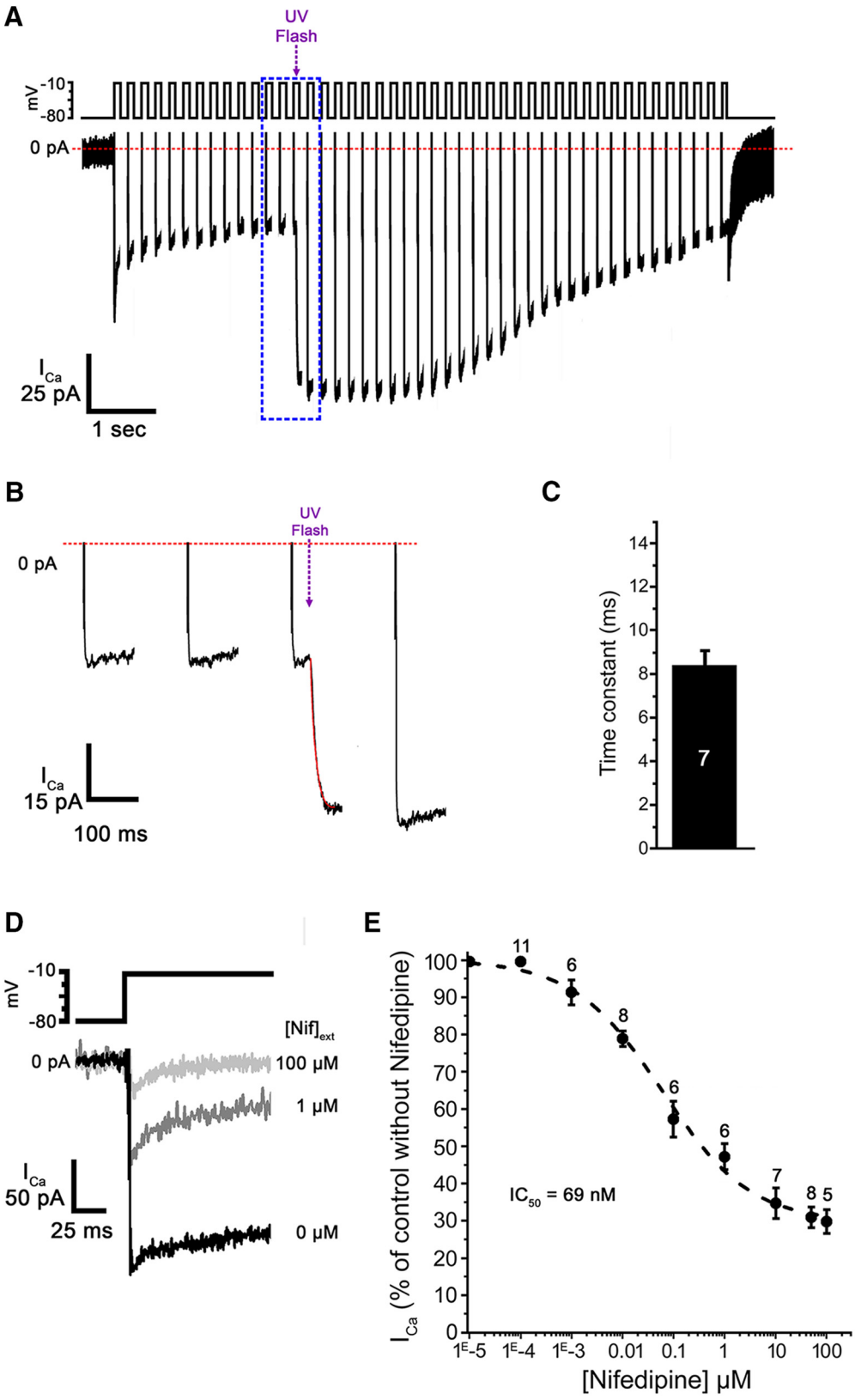

Figure 2. Fast UV reactivation of Ca^{2+} currents in the presence of extracellular nifedipine. ***A***, Example of Ca^{2+} current trace recorded in response to a train of 100 ms stimulation from −80 to −10 mV. The purple arrow indicates the UV flash reactivation of the Ca^{2+} current. ***B***, Magnification from blue dashed box in ***A***. We used a single exponential function (red line) to fit the kinetics of unblocking Ca^{2+} current. Mean kinetics time constants are plotted in ***C***. ***D***, Examples of Ca^{2+} current recorded in response to a 100 ms depolarization from −80 mV to −10 mV in the presence of 0 μM (black trace), 1 μM (dark gray trace), and 100 μM (light gray trace) extracellular nifedipine. ***E***, Dose-inhibitory response curve of nifedipine on the amplitude of IHC Ca^{2+} currents. Data points were fitted with a sigmoidal Hill function with an IC_{50} of 69 nM and $n_{Hill} = 1$. The cell number is indicated above each data point.

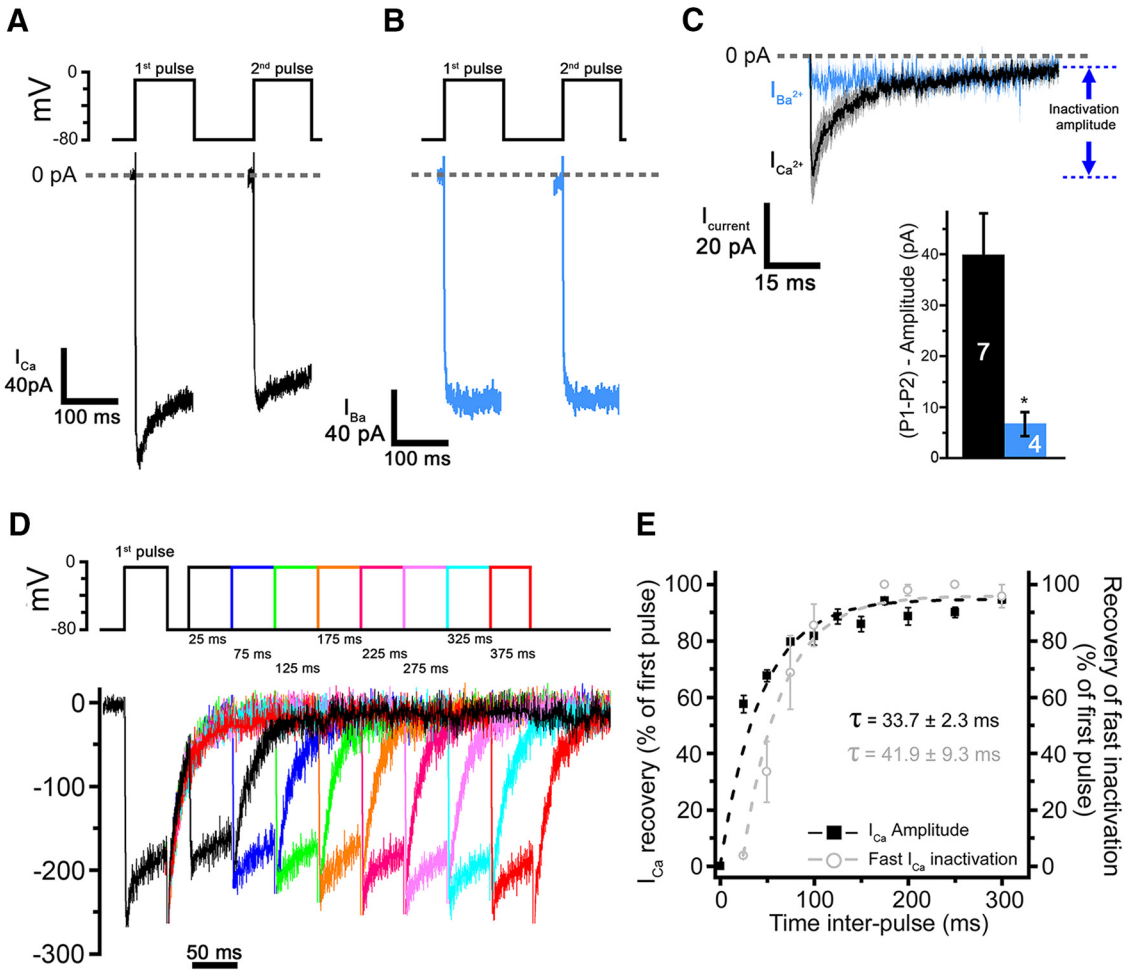

Figure 3. Absence of paired-pulse inactivation of Ba^{2+} currents. ***A***, Paired-pulse protocol of Ca^{2+} currents as in Figure 1. ***B***, Paired-pulse protocol of Ba^{2+} currents when extracellular Ca^{2+} ions were replaced by 5 mM Ba^{2+}. ***C***, Comparative averaged subtracted traces (pulse 1 − pulse 2). ***D***, Ca^{2+} current recordings in response to a paired-pulse protocol (two pulses of 50 ms from −80 to −10 mV) with increasing interpulse durations. The protocol is represented at the top. Each color represents one given interpulse duration. ***E***, Time recovery of the I_{Ca} amplitude (black squares) and the fast-inactivating component (light gray circles) of the Ca^{2+} current ($n = 8$ cells). The I_{Ca} amplitude was measured between the baseline and the maximum peak. The fast-inactivating component was determined with a single exponential from the maximum peak to the steady state of the inactivation. Data point were fitted with a single exponential (dotted lines).

synaptic responses despite being positioned >20 μm away from the synaptic zones, indicating that they were not due to Ca^{2+} diffusion or intracellular release, but rather from Ca^{2+} entry through Ca^{2+} channels. Reinforcing this hypothesis, our confocal immunohistochemistry experiments showed that small $Ca_v1.3$ clusters can indeed be detected below the cuticular area, whereas most Ca^{2+} channels are clustered at the basal synaptic ribbons (Fig. 7*D*). Conversely, in the subcuticular zones, the Ca^{2+} responses measured near the middle of the cell above the nucleus (orange trace) at ~9 μm away from the synaptic base showed a large delay (Δt) in their peak responses: 191 ± 19 ms ($n = 7$) compared with the synaptic responses (Fig. 7*B*,*C*). These Ca^{2+} responses above the nucleus were likely due to Ca^{2+} diffusion from the synaptic zones and the subcuticular area and/or to intracellular store release.

Expression of short and long $Ca_v1.3$ channel isoforms in IHCs

Transcripts of the $Ca_v1.3$ long isoform ($Ca_v1.3_{42L}$) were detected in mature OCs of P20–P35 mice (Fig. 8*A*,*B*). Two short alternative splicing isoforms, 43S ($Ca_v1.3_{43S}$) and 42A ($Ca_v1.3_{42A}$), were also identified. RT-PCR of transcripts collected directly from P18 WT IHCs with a patch pipette also showed the expression of these long and short isoforms of $Ca_v1.3$ at the cellular level (Fig. 8*E*). Q-PCR showed that OCs from P20–P35 *Otof*$^{-/-}$ mice had a reduced transcript expression of $Ca_v1.3_{43S}$ and $Ca_v1.3_{42A}$ short isoforms compared with P20–P35 WT mice (Fig. 8*A*,*C*,*D*), whereas the long isoform $Ca_v1.3_{42L}$ did not show any significant change (data not shown). The reduced expression of $Ca_v1.3_{43S}$ and $Ca_v1.3_{42A}$ short isoforms in the OC of *Otof*$^{-/-}$ mice was confirmed at the protein level by Western blot analysis (Fig. 8*F*,*G*). The protein expression of $Ca_v1.3_{43S}$ (187 kDa) and $Ca_v1.3_{42A}$ (176 kDa), normalized to the vesicular glutamate transporter VGLUT3, was reduced by 21% and 24%, respectively, in the OC of *Otof*$^{-/-}$ mice compared with *Otof*$^{+/+}$. *Otof*$^{-/-}$ IHCs did not show any apparent lack or accumulation of synaptic vesicles (Roux et al., 2006) and VGLUT3 expression remained similar to *Otof*$^{+/+}$ IHCs (Fig. 9*A*). Along with the reduced inactivation of Ca^{2+} current in *Otof*$^{-/-}$ IHCs (Fig. 1*E*,*G*), these results suggest that $Ca_v1.3_{43S}$ and $Ca_v1.3_{42A}$ likely underlie the fast-inactivating and nifedipine-resistant currents described in WT IHCs (Fig. 1*F*). Moreover, we also found transcript coding the long $Ca_v1.3$ isoform deleted for the exon 44 ($Ca_v1.3_{\Delta 44}$; data not shown) in P18 WT IHCs. This long $Ca_v1.3$ isoform was characterized by a fast inactivating rate, but slower than the two short isoforms (Tan et al., 2011).

Mature *Otof*$^{-/-}$ IHCs displayed a nearly 2-fold decrease in the number of ribbons per IHC (19 ± 1 ribbons per cell and 9 ±

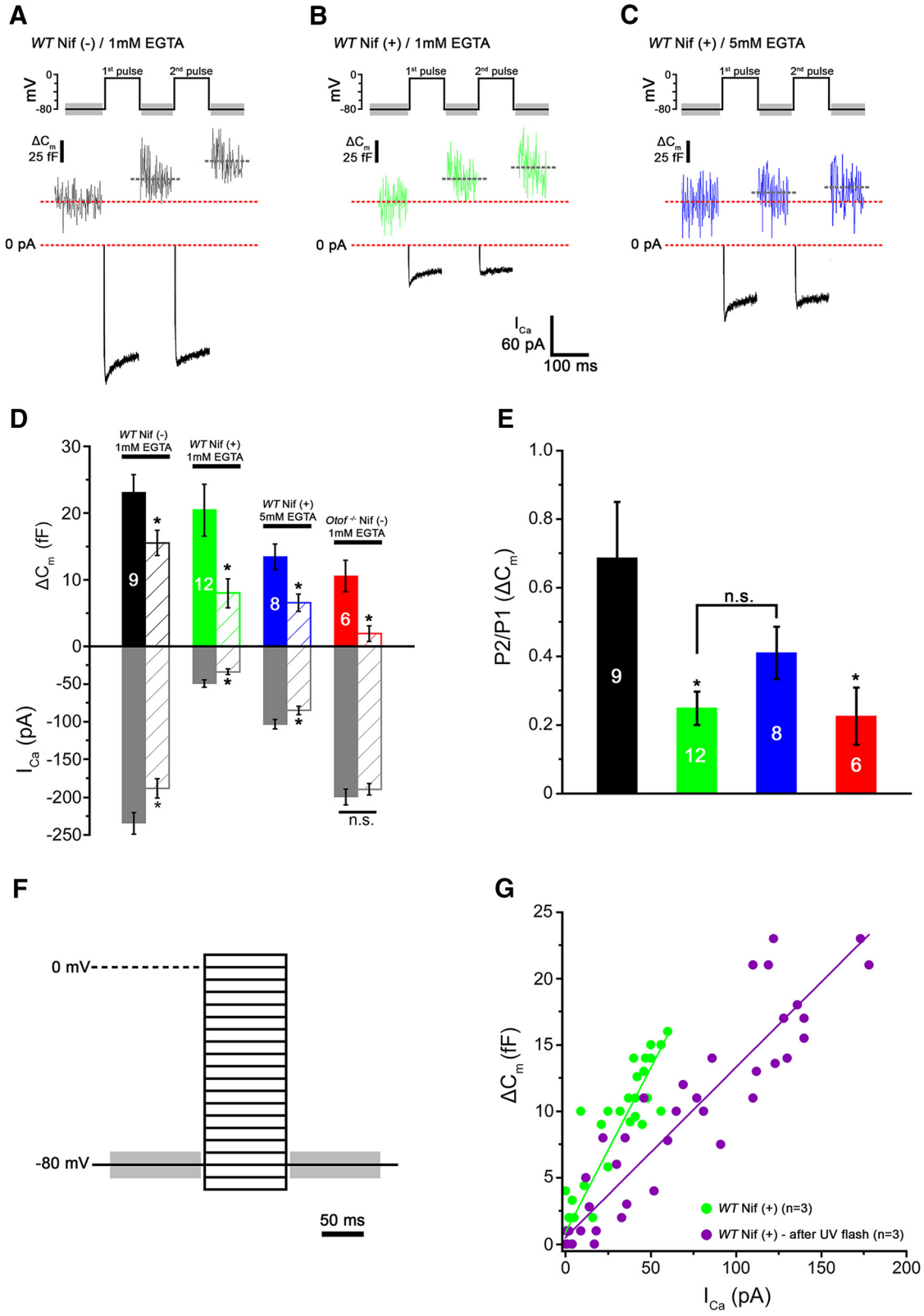

Figure 4. RRP exocytosis is weakly affected by nifedipine. ***A–C***, Examples of capacitance response (Δ_{Cm}, top) and Ca^{2+} currents (bottom) recorded in response to a 100 ms paired-pulse stimulation: control condition (***A***), condition with 20 μM extracellular nifedipine (***B***), and condition with 5 mM intracellular EGTA and 20 μM extracellular nifedipine (***C***). ***D***, Comparative histograms of Δ_{Cm} and Ca^{2+} currents recorded in control condition (black), with nifedipine (green), with nifedipine and 5 mM EGTA (blue), and in *Otof*$^{-/-}$ without nifedipine (red). Filled histograms show data from the first pulse (P1, Δ_{Cm1}) and hatched histograms from the second pulse (P2, Δ_{Cm2}). Δ_{Cm1} was calculated as the difference between responses at P1 and baseline (red dotted line). Δ_{Cm2} was calculated as the difference between responses at P2 and P1. ***E***, Comparative histograms of Δ_{Cm} P2/P1 ratio. ***F***, ***G***, Ca^{2+} efficiency of RRP exocytosis in response to various voltage steps (100 ms duration, from −80 mV to +5 mV in 5 mV increments; ***F***) in the presence of 20 μM nifedipine before (green) and after UV-unblocking Ca^{2+} currents (purple) in WT IHCs. Error bars indicate SEM. Nif (−) indicates condition without nifedipine and Nif (+) condition with 20 μM nifedipine. *$p < 0.05$.

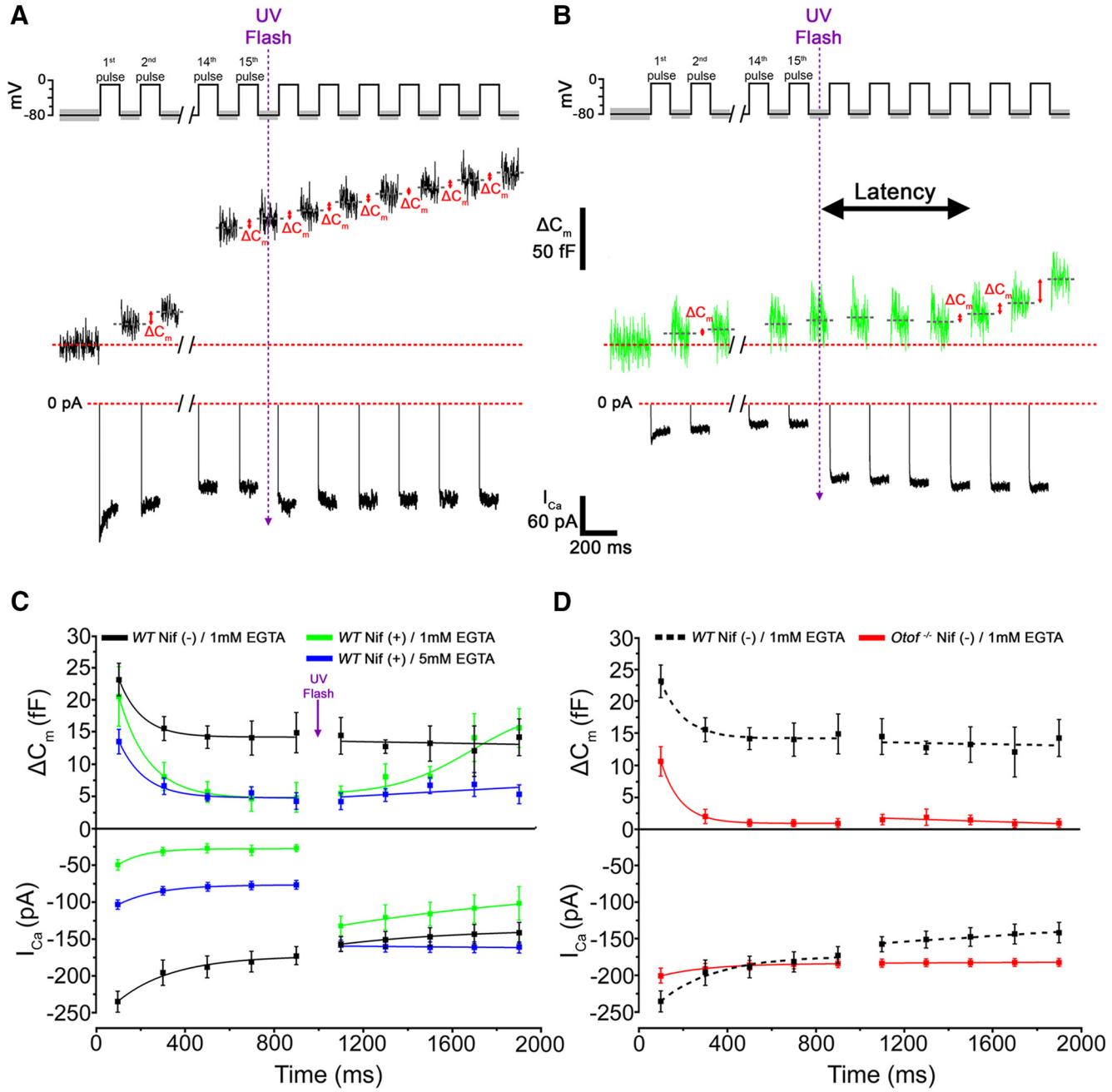

Figure 5. Nifedipine greatly reduces sustained exocytosis. Examples of comparative changes in Δ_{Cm} and Ca^{2+} currents in control condition (***A***) and in the presence of 20 μM extracellular nifedipine (***B***) when applying a train of 100 ms stimulations. Dashed purple arrows indicate the illumination with UV. ***C***, Plot of the sequential, 5 first, mean Δ_{Cm}, and Ca^{2+} current responses before and after the UV flash: control condition (black), condition with 20 μM nifedipine (green), condition with EGTA (5 mM) and nifedipine (blue). ***D***, Similar comparative plot in control condition for WT IHCs (black dashed line) and *Otof*$^{-/-}$ IHCs (red). Note the latency of the Δ_{Cm} response after UV-unblocking Ca^{2+} channels in the presence of nifedipine (***B***, ***C***). Error bars indicate SEM.

2 ribbons in P16-*Otof*$^{+/-}$ and P16-*Otof*$^{-/-}$ IHC, respectively; $p < 0.05$; Fig. 8 *F*, *G*). The mean surface area of the ribbons was also decreased in *Otof*$^{-/-}$ IHCs (Fig. 8*H*; 4.6 ± 0.1 μm^2 and 3.3 ± 0.1 μm^2, *Otof*$^{+/-}$ and *Otof*$^{-/-}$; $p < 0.05$). These results suggest that otoferlin is required for both the expression of the short $Ca_v1.3$ isoforms and the organization of normal ribbons in IHCs.

Discussion

IHCs use $Ca_v1.3$ long and short isoforms for fine control of synaptic transmission

Here, we show that posthearing IHCs express a fast-inactivating nifedipine-resistant Ca^{2+} current that represents 25% of the total Ca^{2+} current. The $V_{1/2}$ of this current was established at ~−28 mV, thus excluding the implication of T-type Ca^{2+} channels that are characterized by a higher negative activation range (Carbone et al., 2014). T-type channels are believed to be expressed only in prehearing immature hair cells (Levic et al., 2007; Levic and Dulon, 2012). Moreover, the absence of fast inactivation in the presence of Ba^{2+} also argues against the implication of this Ca^{2+} channel family. Indeed, T-type Ca^{2+} channels are known to display a strong and fast inactivation even after Ba^{2+} replaces Ca^{2+} (Lacinova, 2005). A transient proton-mediated block of Ca^{2+} channels has been described during exocytosis in auditory

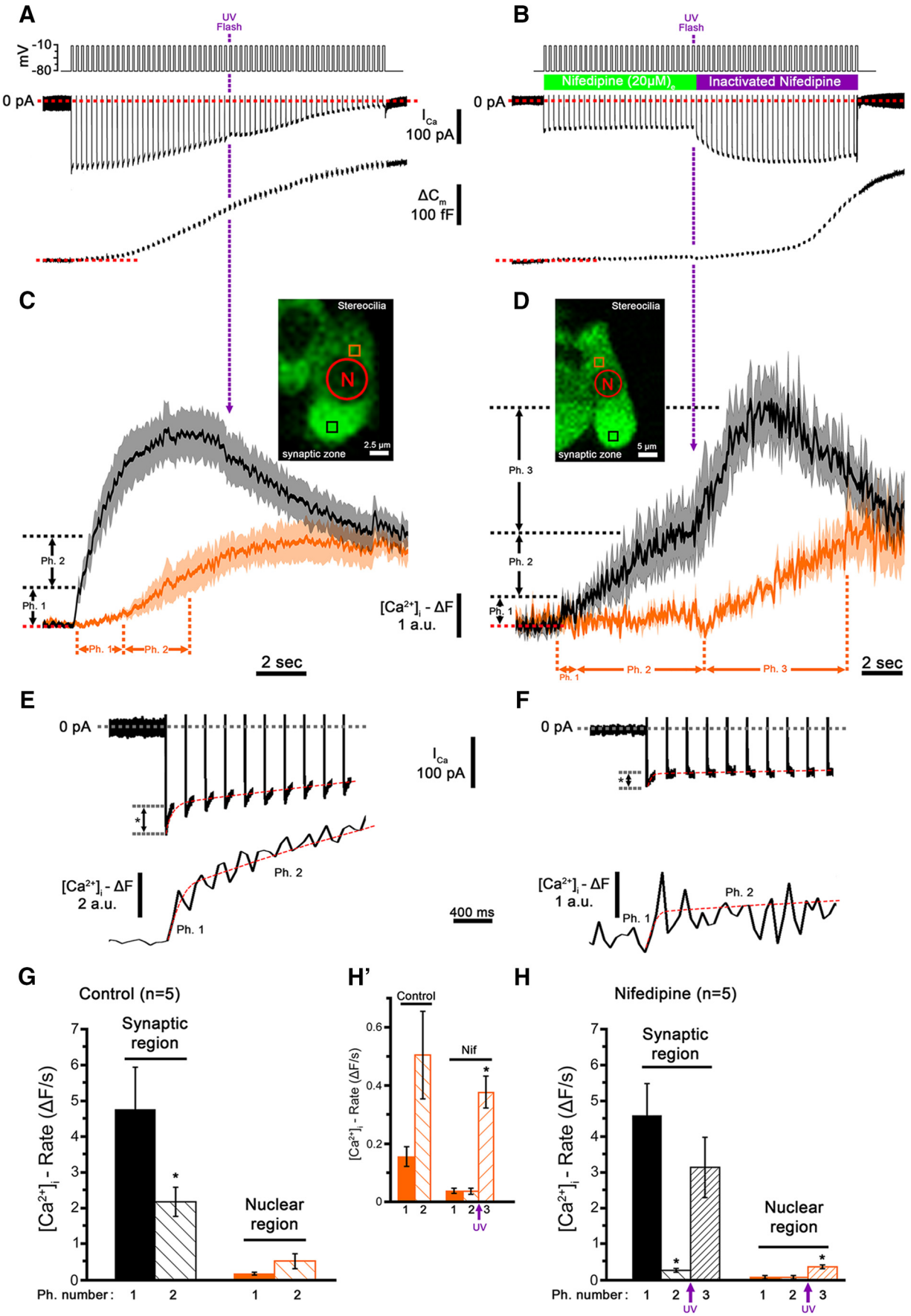

Figure 6. Ca^{2+} imaging during a train of stimuli reveals a fast synaptic response and a delayed, slowly developing extrasynaptic response in the region right above the nucleus. ***A***, ***B***, Examples of simultaneous recording of Ca^{2+} current (top) and capacitance response (bottom) in control condition (***A***) and in the presence of 20 μM nifedipine (***B***) for WT IHCs during a (*Figure legend continues.*)

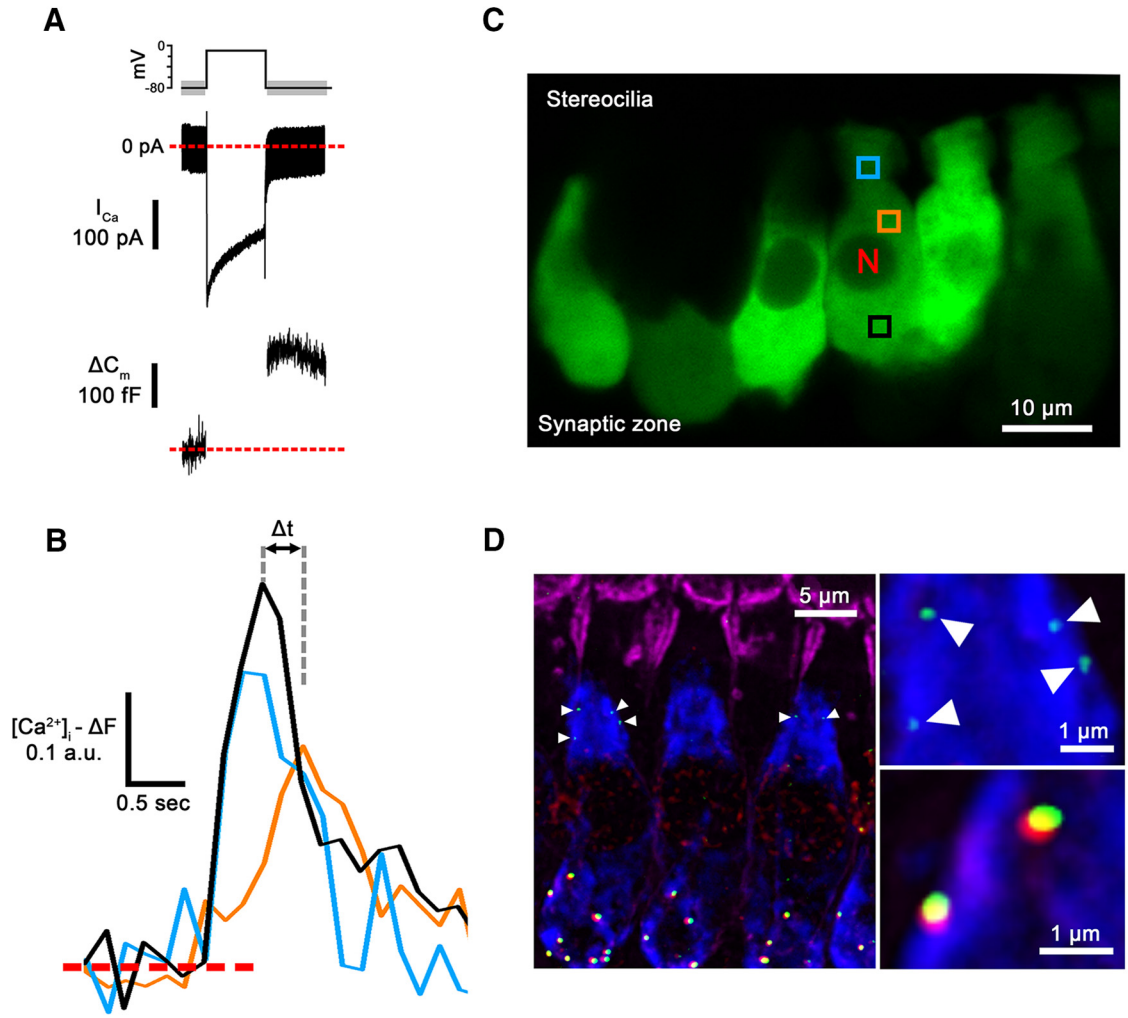

Figure 7. Ca^{2+} imaging and immunohistochemistry mostly localize $Ca_v1.3$ Ca^{2+} channels at the synaptic ribbons of WT IHCs but small $Ca_v1.3$ clusters are also seen extrasynaptically right below the cuticular plate region. ***A***, ***B***, Example of simultaneous recording of Ca^{2+} current (top) and capacitance response (bottom) in control condition (***A***) in a WT IHC evoked during a single 500 ms step depolarization from −80 mV to −10 mV. A simultaneous intracellular Ca^{2+} increase was recorded through the fast Ca^{2+} indicator, GCamP6f (***B***, ***C***). Ca^{2+} signals were measured from the synaptic zone (black line), above the nucleus (orange line), and under the cuticular plate region (blue line) as indicated in ***C***, showing a row of IHCs genetically expressing the Ca^{2+} indicator GCamP6f. Boxes represent the ROI used for the Ca^{2+} measurement shown in ***B***. Δt represents the time difference between the maximum peak of intracellular Ca^{2+} measured at the synaptic area and the region above the nucleus. ***D***, Typical example of $Ca_v1.3$ immunolabeling at the apical turn of a whole-mount OC from a P14 mouse. F-actin is labeled in pink, otoferlin in blue, CtBP2 (ribbon) in red, and Cav1.3 in green. Right top panel shows the cuticular plate region at higher magnification and the small clusters of $Ca_v1.3$ (arrowheads). Right bottom panel shows two synaptic active zones at higher magnification.

←

(*Figure legend continued.*) train of 100 ms stimulations from −80 mV to −10 mV. Simultaneous intracellular Ca^{2+} increase (mean ± SEM) was recorded in IHCs expressing the fast Ca^{2+} indicator GCamP6f in control condition (***C***) and in the presence of nifedipine (***D***). Insets in ***C*** and ***D*** show examples of fluorescent IHCs expressing GCamP6f. Black and orange boxes are the selected ROI for fluorescence measurements at the synaptic and subcuticular plate regions, respectively. Purple arrows and dotted lines represent the timing of UV-unblocking Ca^{2+} channels. The red circle with "N" indicates the position of the nucleus. Superimposed Ca^{2+} currents (top) and synaptic intracellular Ca^{2+} measurement (bottom) are shown during the first 10 stimuli for control condition (***E***) and nifedipine condition (***F***). Note that the fast-transient-inactivating component of Ca^{2+} current (asterisk) coincided with the first phase (Ph1) of Ca^{2+} increase, whereas the second phase (Ph2) mirrored the sustained Ca^{2+} current. Comparative histograms of the rates of Ca^{2+} increase in the basal synaptic region (SR) and above the nuclear region (NR) in control and nifedipine conditions are shown in ***G*** and ***H***, respectively. Ph1, Ph2, and Ph3, Phase numbers 1, 2, and 3 (post-UV) in ***C*** and ***D***, respectively. Rates were obtained by fitting Ph1, Ph2, and Ph3 with a linear function. ***H′***, Magnification of the Ph1, Ph2, and Ph3 (post-UV) responses recorded at the subcuticular plate region shown in ***G*** and ***H*** in control and nifedipine conditions. $*p < 0.05$.

bullfrog hair cells (Cho and von Gersdorff, 2014). However, the Ca^{2+} current inactivation described here is unlikely to be due to a proton effect because we were working with 10 mM extracellular HEPES buffer, a concentration that prevents pH variations at the synaptic cleft of bullfrog auditory hair cells (Cho and von Gersdorff, 2014). The fast-inactivating nifedipine-resistant Ca^{2+} current uncovered in our study is essentially conducted by $Ca_v1.3$ channels. Indeed, $Ca_v1.3^{-/-}$ IHCs display <10% of WT Ca^{2+}current and this residual current does not show inactivation (Platzer et al., 2000; Brandt et al., 2003 see their Figs. 3*F* and 1*A*, respectively). Our results also suggest that the fast-inactivating nifedipine-resistant Ca^{2+} currents are driven by the $Ca_v1.3$ short isoforms 42A and 43S, the transcripts of which were found to be strongly expressed in IHCs. In agreement with our study, the $Ca_v1.3$ short isoform 43S transcript was shown recently to be expressed in IHCs (Scharinger et al., 2015). Expression in a heterologous system of these short $Ca_v1.3$ isoforms displays Ca^{2+} currents with similar fast inactivation and reduced sensitivity to nifedipine (Singh et al.,

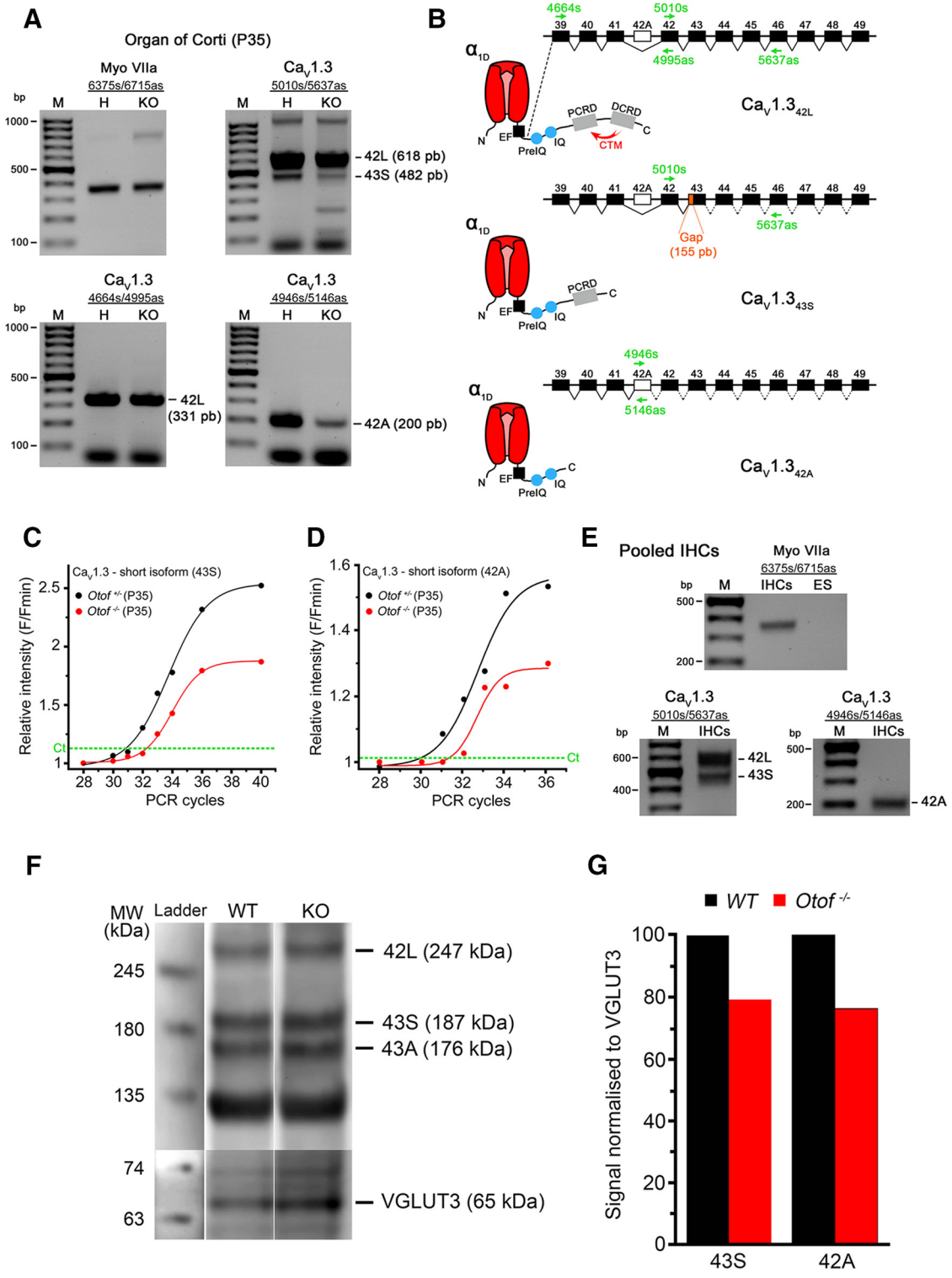

Figure 8. Transcript mRNA expression of $Ca_V1.3$ short and long isoforms. ***A***, RT-PCR expression of myosin VIIa (Myo VIIa, top left), 42L isoform (long Cav1.3 isoform, bottom left) using 4664s/4995as, both 43S and 42L isoforms using 5010s/5637as (top right) and 42A (bottom right) using 4946s/5146as in P35 *Otof* $^{+/-}$ (heterozygous: H) and *Otof* $^{-/-}$ (KO) OCs. ***B***, Schematic presentation of alternative splicing of Cav1.3 C terminus (c-term) domain for long isoform 42L (top), short isoform 43S (middle), and short isoform 42A (bottom). Black and blank rectangles represent constitutive and alternative splicing, respectively. Incorporation of exon 42A instead of exon 42 induces a premature nonsense codon leading to a truncated c-term domain. Orange box represents the lack of 155 nt in the 43S sequence inducing a premature nonsense codon and a truncated c-term domain. Under each sequence, a schematic drawing of the translated α_{1D} c-term domain controlling Ca^{2+}-dependent inactivation is shown. The red arrow (top schematic drawing) indicates the formation of the CTM by the interaction between the PCRD and DCRD for the long 42L isoform. Such a regulatory domain cannot be formed in the case of the two short 43S and 42A isoforms. Note that the green arrows above and under each sequence represent the hybridization site for each used primer. ***C***, ***D***, Q-PCR from P35 *Otof* $^{+/-}$ (black) and *Otof* $^{-/-}$ (red) OCs for short isoforms 43S (***C***) and 42A (***D***). Green dotted line represents the Ct. ***E***, RT-PCR from pooled WT IHCs shows the transcripts of short (43S and 42A) and long (42L) Cav1.3 isoforms. ES: Extracellular solution was used as negative control. ***F***, ***G***, Western blot analysis indicating a reduction of 43S and 42A Cav1.3 isoforms in *Otof* $^{-/-}$ OC.

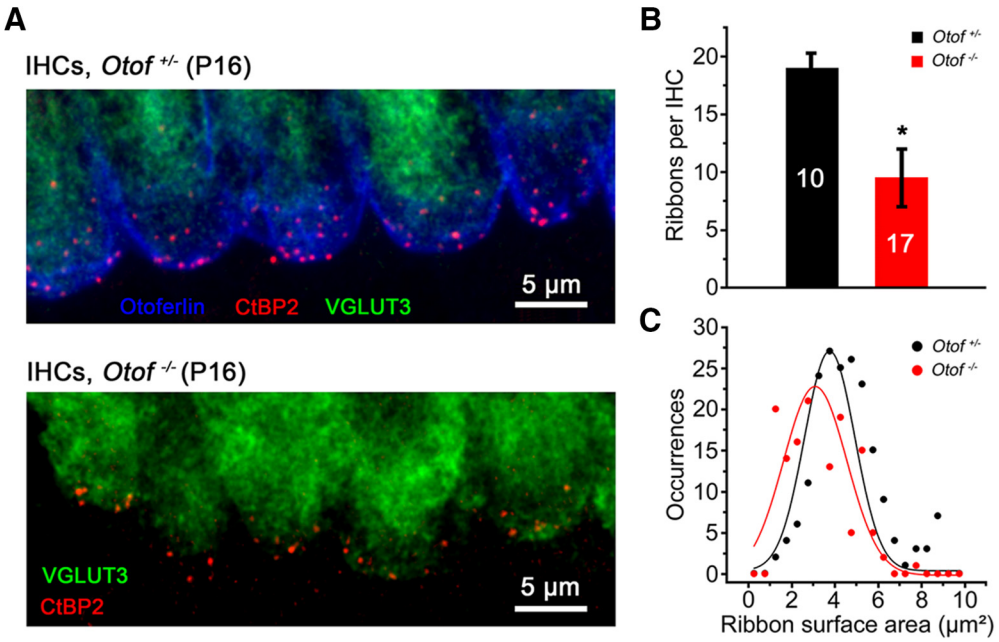

Figure 9. Comparison of ribbon immunolabeling between *Otof* $^{+/-}$ and *Otof* $^{-/-}$ mice. ***A***, Stack-reconstructed confocal images from P16 *Otof* $^{+/-}$ and *Otof* $^{-/-}$ IHCs at the apical turn of OC. Tissues were immunolabeled for CtBP2 (ribbons; red), otoferlin (blue), and VGLUT-3 (green). ***B***, ***C***, Comparative number of ribbons per cell (***B***) and distribution of ribbon surface area (***C***) in *Otof* $^{+/-}$ (black) and *Otof* $^{-/-}$ (red) IHCs. *$p < 0.05$.

2008; Bock et al., 2011; Huang et al., 2013). The implication of these short $Ca_v1.3$ isoforms in IHCs was further reinforced in our study by the concomitant decrease of the fast-inactivating component of the Ca^{2+} current and the reduced expression of the $Ca_v1.3_{42A}$ and $Ca_v1.3_{43S}$ in IHCs lacking otoferlin.

Remarkably, we found that the nifedipine-resistant Ca^{2+} current could still trigger a very efficient RRP exocytotic response when a short depolarizing pulse was applied. However, this exocytotic response showed a large depression during a paired-pulse or a train protocol. These results suggest that the fast-inactivating nifedipine-resistant Ca^{2+} channels are mainly involved in the release of RRP composed of ribbon associated vesicles, whereas the nifedipine-sensitive Ca^{2+} channels allowing deep intracellular diffusion of Ca^{2+} mainly control vesicular recruitment (SRP). Our results are in good agreement with previous studies showing the Ca^{2+} dependence of vesicular recruitment in hair cells (Cho et al., 2011; Levic et al., 2011; Schnee et al., 2011).

C-terminal domain of $Ca_v1.3$ channels shapes the inactivation kinetics

The C-terminal region of the $Ca_v1.3$ subunit contains regulatory domains that control calcium-dependent inactivation (CDI). This process occurs when the four EF-hand Ca^{2+} sensing protein calmodulin (CaM) interacts with the IQ and pre-IQ domains (Peterson et al., 1999; Qin et al., 1999; Erickson et al., 2003; Liu et al., 2010; Catterall, 2011; Striessnig et al., 2014). Calmodulin-like calcium-binding proteins (CaBPs), which have been found expressed to be in chick (Lee et al., 2007), mouse (Cui et al., 2007) and rat (Yang et al., 2006) auditory hair cells, can also regulate the CDI kinetics by competing with CaM interaction at the IQ domain (Lee et al., 2002; Yang et al., 2006; Cui et al., 2007; Striessnig et al., 2014). Multiple CaBPs isoforms are expressed in IHCs, notably CaBP1 and CaBP2, which are well colocalized at the IHC ribbon synapse (Cui et al., 2007). In addition, at the extreme C terminus of $Ca_v1.3$ long isoforms, two α helix proximal (PCRD) and distal C-terminal regulatory domains (DCRD; Fig. 8*B*) interact with each other to form the C-terminal regulatory domain (CTM; Fig. 8*B*, red arrow). This CTM domain is thought to slow down the inactivation kinetics of long $Ca_v1.3$ isoforms by competing with the interaction of the Ca^{2+}–CaM and IQ domains (Singh et al., 2008; Liu et al., 2010, Striessnig et al., 2014). The exon 44 encodes ~10 aa between PCRD and DCRD (Tan et al., 2011). The absence of these 10 aa shortened the length between these two domains and led to faster inactivation kinetics than the long $Ca_v1.3_{42L}$ isoform but slower than the two $Ca_v1.3_{42A}$ and $Ca_v1.3_{43S}$ short isoforms (Bock et al., 2011; Tan et al., 2011). The speed up of the $Cav1.3_{\Delta 44}$ inactivation compared with the long $Cav1.3_{42L}$ isoform could be the result of a misfolding between the PCRD and the DCRD reinforcing the strength of the CDI. Although the short isoforms, $Ca_v1.3_{42A}$ and $Ca_v1.3_{43S}$, lack the two last domains PCRD and DCRD or only the DCRD domain, respectively, they still possess the pre-IQ and IQ domains for Ca^{2+}–CaM regulation (Huang et al., 2013). These truncated C-terminal regulatory domains in $Ca_v1.3_{42A}$ and $Ca_v1.3_{43S}$ channels is likely to explain their peculiar fast-inactivating kinetics in the millisecond range (Singh et al., 2008; Bock et al., 2011; Tan et al., 2011; Huang et al., 2013). The nifedipine-resistant Ca^{2+} current of IHCs displayed similar fast inactivation kinetics, suggesting that it could be driven by the $Ca_v1.3_{42A}$ and $Ca_v1.3_{43S}$ isoforms. Notably, the total Ca^{2+} current in IHCs displayed a small fast-inactivating component (with $t \sim 4$–5 ms) and a second, large, slowly inactivating component (with $\tau \sim 65$ ms; data not shown), in agreement with results obtained in turtle auditory hair cells (Schnee and Ricci, 2003). This second slow-inactivating component, which is sensitive to nifedipine, likely corresponds to the slow inactivation of the $Ca_v1.3_{42L}$ long isoform (bearing 75% of total Ca^{2+} current) that conserves intact PCRD and DCRD domains (Fig. 8*B*).

Reduced expression of $Ca_v1.3_{42A}$ and $Ca_v1.3_{43S}$ isoforms in *Otof* $^{-/-}$ IHCs

In *Otof* $^{-/-}$ IHCs, we found that expression of $Ca_v1.3_{42A}$ and $Ca_v1.3_{43S}$ transcripts is decreased and associated with a large-

amplitude reduction in the fast-inactivating Ca^{2+} currents. As shown previously by Roux et al. (2006), we found a 50% decrease in the number of synaptic ribbons in *Otof*$^{-/-}$ IHCs. Otoferlin thus appears essential, not only for sensing Ca^{2+} and preserving ribbons at the presynaptic active zones, but also for maintaining a strong expression of the $Ca_v1.3_{42A}$ and $Ca_v1.3_{43S}$ channels. Disruption of the ribbon-associated cytomatrix protein bassoon in IHCs has also been shown to generate a loss of synaptic ribbons and a concomitant reduction in $Ca_v1.3$ channel expression (Frank et al., 2010). The reduction in the number of ribbons and the concomitant decrease in Ca^{2+} current inactivation observed in our study suggest that the $Ca_v1.3_{42A}$ and $Ca_v1.3_{43S}$ channels are functionally associated with the synaptic ribbons in IHCs.

Gain of using various $Ca_v1.3$ isoforms during IHC exocytosis

Auditory IHCs are remarkable in that they encode sound timing information precisely up to several kilohertz into phase-locked specific afferent discharge rates (Palmer and Russell, 1986). Presynaptic $Ca_v1.3$ short isoforms, inactivating in the millisecond range, would certainly be crucial for ensuring high-frequency phase locking and rapid adaptation of the afferent discharge rate. In central neurons (Tan et al., 2011) and in heart pacemaker cells (Bock et al., 2011), short $Ca_v1.3$ isoforms are believed to limit Ca^{2+} accumulation during fast-bursting activity. In IHCs, these short isoforms might help to reduce the size of Ca^{2+} domains below the synaptic ribbons. Notably, the ribbons themselves with their docked vesicles placed near the Ca^{2+} channels could further limit intracellular Ca^{2+} diffusion by acting as a diffusion barrier (Graydon et al., 2011). Conversely, slowly inactivating long $Ca_v1.3$ isoforms might allow a sustained and deeper Ca^{2+} diffusion in IHCs (Liu et al., 2010), a property essential for recruiting vesicles at large distances from the release sites. We propose that Ca^{2+} microdomains of IHCs may be composed of various proportions of long and short $Ca_v1.3$ isoforms that could lead to the observed heterogeneity of the Ca^{2+} signal between active zones (Frank et al., 2009).

Extrasynaptic Ca^{2+} channels at the subcuticular zone of IHCs

We also show here for the first time strong evidence for extrasynaptic $Ca_v1.3$ channel clusters below the cuticular plate, where BK channels (Pyott et al., 2004; Hafidi et al., 2005) and ryanodine receptors (Beurg et al., 2005) have been shown previously to be strongly expressed in IHCs. Their blockage by nifedipine suggested that they mainly involve $Ca_v1.3$ long isoforms. What is the physiological role for these apical $Ca_v1.3$ Ca^{2+} channel clusters? They could possibly trigger calcium-induced calcium release from intracellular Ca^{2+} stores (Beurg et al., 2005; Castellano-Muñoz and Ricci, 2014) and regulate the fast-repolarizing Ca^{2+}-dependent BK currents in IHCs (Skinner et al., 2003; Beurg et al., 2005). Remarkably, IHCs have been proposed to contain two specialized areas of membrane delivery, the basal synaptic ribbons and the subcuticular area, where SNARE proteins are concentrated (Safieddine and Wenthold, 1999; Safieddine et al., 2002). It is therefore possible that the subcuticular $Ca_v1.3$ Ca^{2+} channels could regulate Ca^{2+}-dependent apical extrasynaptic exo–endocytotic processes, as was suggested previously in the zebrafish's lateral line (Seiler and Nicolson, 1999) and in vestibular hair cells of the bull frog (Kachar et al., 1997). This process has been proposed to underlie communication between the endolymphatic compartment and IHC cytoplasm (Kachar et al., 1997; Seiler and Nicolson, 1999), but also to regulate the Ca^{2+} and calmodulin-dependent adaptation mechanism of the hair bundles by sequestrating the Ca^{2+} ATPase (Seiler and Nicolson, 1999).

References

Beurg M, Hafidi A, Skinner LJ, Ruel J, Nouvian R, Henaff M, Puel JL, Aran JM, Dulon D (2005) Ryanodine receptors and BK channels act as a presynaptic depressor of neurotransmission in cochlear inner hair cells. Eur J Neurosci 22:1109–1119. CrossRef Medline

Beurg M, Michalski N, Safieddine S, Bouleau Y, Schneggenburger R, Chapman ER, Petit C, Dulon D (2010) Control of exocytosis by synaptotagmins and otoferlin in auditory hair cells. J Neurosci 30:13281–13290. CrossRef Medline

Bock G, Gebhart M, Scharinger A, Jangsangthong W, Busquet P, Poggiani C, Sartori S, Mangoni ME, Sinnegger-Brauns MJ, Herzig S, Striessnig J, Koschak A (2011) Functional properties of a newly identified C-terminal splice variant of Cav1.3 L-type Ca2+ channels. J Biol Chem 286:42736–42748. CrossRef Medline

Brandt A, Striessnig J, Moser T (2003) Ca(V)1.3 channels are essential for development and presynaptic activity of cochlear inner hair cells. J Neurosci 23:10832–10840. Medline

Brandt A, Khimich D, Moser T (2005) Few Ca(V)1.3 channels regulate the exocytosis of a synaptic vesicle at the hair cell ribbon synapse. J Neurosci 25:11577–11585. CrossRef Medline

Carbone E, Calorio C, Vandael DH (2014) T-type channel-mediated neurotransmitter release. Pflugers Arch 466:677–687. CrossRef Medline

Castellano-Muñoz M, Ricci AJ (2014) Role of intracellular calcium stores in hair-cell ribbon synapse. Front Cell Neurosci 8:162. CrossRef Medline

Catterall WA (2011) Voltage-gated calcium channels. Cold Spring Harb Perspect Biol 3:a003947. CrossRef Medline

Chen TW, Wardill TJ, Sun Y, Pulver SR, Renninger SL, Baohan A, Schreiter ER, Kerr RA, Orger MB, Jayaraman V, Looger LL, Svoboda K, Kim DS (2013) Ultrasensitive fluorescent proteins for imaging neuronal activity. Nature 499:295–300. CrossRef Medline

Cho S, von Gersdorff H (2014) Proton-mediated block of Ca^{2+} channels during multivesicular release regulates short-term plasticity at an auditory hair cell synapse J Neurosci 34:15877–15887. CrossRef

Cho S, Li GL, von Gersdorff H (2011) Recovery from short-term depression and facilitation is ultrafast and Ca2+ dependent at auditory hair cell synapses. J Neurosci 31:5682–5692. CrossRef Medline

Cui G, Meyer AC, Calin-Jageman I, Neef J, Haeseleer F, Moser T, Lee A (2007) Ca2+-binding proteins tune Ca2+-feedback to Cav1.3 channels in mouse auditory hair cells. J Physiol 585:791–803. CrossRef Medline

Erickson MG, Liang H, Mori MX, Yue DT (2003) FRET two-hybrid mapping reveals function and location of L-type Ca2+ channel CaM preassociation. Neuron 39:97–107. CrossRef Medline

Feldmeyer D, Zöllner P, Pohl B, Melzer W (1995) Calcium current reactivation after flash photolysis of nifedipine in skeletal muscle fibres of the frog. J Physiol 487:51–56. CrossRef Medline

Frank T, Khimich D, Neef A, Moser T (2009) Mechanisms contributing to synaptic Ca2+ signals and their heterogeneity in hair cells. Proc Natl Acad Sci U S A 106:4483–4488. CrossRef Medline

Frank T, Rutherford MA, Strenzke N, Neef A, Pangršič T, Khimich D, Fetjova A, Gundelfinger ED, Liberman MC, Harke B, Bryan KE, Lee A, Egner A, Riedel D, Moser T (2010) Bassoon and the synaptic ribbon organize Ca(2)+ channels and vesicles to add release sites and promote refilling. Neuron 68:724–738. CrossRef Medline

Grant L, Fuchs P (2008) Calcium- and calmodulin-dependent inactivation of calcium channels in inner hair cells of the rat cochlea. J Neurophysiol 99:2183–2193. CrossRef Medline

Graydon CW, Cho S, Li GL, Kachar B, von Gersdorff H (2011) Sharp Ca^{2+} nanodomains beneath the ribbon promote highly synchronous multivesicular release at hair cell synapses. J Neurosci 31:16637–16650. CrossRef Medline

Hafidi A, Beurg M, Dulon D (2005) Localization and developmental expression of BK channels in mammalian cochlear hair cells. Neuroscience 130:475–484. CrossRef Medline

Huang H, Yu D, Soong TW (2013) C-terminal alternative splicing of CaV1.3 channels distinctively modulates their dihydropyridine sensitivity. Mol Pharmacol 84:643–653. CrossRef Medline

Johnson SL, Marcotti W, Kros CJ (2005) Increase in efficiency and reduction in Ca2+ dependence of exocytosis during development of mouse inner hair cells. J Physiol 563:177–191. CrossRef Medline

Kachar B, Battaglia A, Fex J (1997) Compartmentalized vesicular traffic around the hair cell cuticular plate. Hear Res 107:102–112. CrossRef Medline

Kiang NY (1965) Discharge patterns of single fibers in the cat's auditory nerve. Cambridge, MA: MIT.

Kushmerick C, Renden R, von Gersdorff H (2006) Physiological temperatures reduce the rate of vesicle pool depletion and short-term depression via an acceleration of vesicle recruitment. J Neurosci 26:1366–1377. CrossRef Medline

Lacinova L (2005) Voltage-dependent calcium channels. Gen Physiol Biophys 1–78. Medline

Lee A, Westenbroek RE, Haeseleer F, Palczewski K, Scheuer T, Catterall WA (2002) Differential modulation of Ca(v)2.1 channels by calmodulin and Ca2+-binding protein 1. Nat Neurosci 5:210–217. Medline

Lee S, Briklin O, Hiel H, Fuchs P (2007) Calcium-dependent inactivation of calcium channels in cochlear hair cells of the chicken. J Physiol 583:909–922. CrossRef Medline

Levic S, Dulon D (2012) The temporal characteristics of Ca2+ entry through L-type and T-type Ca2+ channels shape exocytosis efficiency in chick auditory hair cells during development. J Neurophysiol 108:3116–3123. CrossRef Medline

Levic S, Nie L, Tuteja D, Harvey M, Sokolowski BH, Yamoah EN (2007) Development and regeneration of hair cells share common functional features. Proc Natl Acad Sci U S A 104:19108–19113. CrossRef Medline

Levic S, Bouleau Y, Dulon D (2011) Developmental acquisition of a rapid calcium-regulated vesicle supply allows sustained high rates of exocytosis in auditory hair cells. Plos One 6.

Liu X, Yang PS, Yang W, Yue DT (2010) Enzyme-inhibitor-like tuning of Ca(2+) channel connectivity with calmodulin. Nature 463:968–972. CrossRef Medline

Michna M, Knirsch M, Hoda JC, Muenkner S, Langer P, Platzer J, Striessnig J, Engel J (2003) Cav1.3 (alpha 1D) Ca2+ currents in neonatal outer hair cells of mice J Physiol 553:747–758. CrossRef

Morad M, Goldman YE, Trentham DR (1983) Rapid photochemical inactivation of Ca2+-antagonists shows that Ca2+ entry directly activates contraction in frog heart. Nature 304:635–638. CrossRef Medline

Moser T, Beutner D (2000) Kinetics of exocytosis and endocytosis at the cochlear inner hair cell afferent synapse of the mouse. Proc Natl Acad Sci U S A 97:883–888. CrossRef Medline

Nouvian R (2007) Temperature enhances exocytosis efficiency at the mouse inner hair cell ribbon synapse. J Physiol 584:535–542. CrossRef Medline

Palmer AR, Russell IJ (1986) Phase-locking in the cochlear nerve of the guinea-pig and its relation to the receptor potential of inner hair-cells. Hear Res 24:1–15. CrossRef Medline

Pangrsic T, Lasarow L, Reuter K, Takago H, Schwander M, Riedel D, Frank T, Tarantino LM, Bailey JS, Strenzke N, Brose N, Müller U, Reisinger E, Moser T (2010) Hearing requires otoferlin-dependent efficient replenishment of synaptic vesicles in hair cells. Nat Neurosci 13:869–876. CrossRef Medline

Peterson BZ, DeMaria CD, Adelman JP, Yue DT (1999) Calmodulin is the Ca2+ sensor for Ca2+-dependent inactivation of L-type calcium channels. Neuron 22:549–558. CrossRef Medline

Pignier C, Potreau D (2000) Characterization of nifedipine-resistant calcium current in neonatal rat ventricular cardiomyocytes. Am J Physiol Heart Circ Physiol 279:H2259–H2268. Medline

Platzer J, Engel J, Schrott-Fischer A, Stephan K, Bova S, Chen H, Zheng H, Striessnig J (2000) Congenital deafness and sinoatrial node dysfunction in mice lacking class D L-type Ca2+ channels. Cell 102:89–97. CrossRef Medline

Pyott SJ, Glowatzki E, Trimmer JS, Aldrich RW (2004) Extrasynaptic localization of inactivating calcium-activated potassium channels in mouse inner hair cells. J Neurosci 24:9469–9474. CrossRef Medline

Qin N, Olcese R, Bransby M, Lin T, Birnbaumer L (1999) Ca2+-induced inhibition of the cardiac Ca2+ channel depends on calmodulin. Proc Natl Acad Sci U S A 96:2435–2438. CrossRef Medline

Ramakrishnan NA, Drescher MJ, Drescher DG (2009) Direct interaction of otoferlin with syntaxin 1A, SNAP-25, and the L-type voltage-gated calcium channel Cav1.3. J Biol Chem 284:1364–1372. CrossRef Medline

Roux I, Safieddine S, Nouvian R, Grati M, Simmler MC, Bahloul A, Perfettini I, Le Gall M, Rostaing P, Hamard G, Triller A, Avan P, Moser T, Petit C (2006) Otoferlin, defective in a human deafness form, is essential for exocytosis at the auditory ribbon synapse. Cell 127:277–289. CrossRef Medline

Safieddine S, Wenthold RJ (1999) SNARE complex at the ribbon synapses of cochlear hair cells: analysis of synaptic vesicle- and synaptic membrane-associated proteins. Eur J Neurosci 11:803–812. CrossRef Medline

Safieddine S, Ly CD, Wang YX, Wang CY, Kachar B, Petralia RS, Wenthold RJ (2002) Ocsyn, a novel syntaxin-interacting protein enriched in the subapical region of inner hair cells. Mol Cell Neurosci 20:343–353. CrossRef Medline

Sanguinetti MC, Kass RS (1984) Photoalteration of calcium channel blockade in the cardiac Purkinje fiber. Biophys J 45:873–880. CrossRef Medline

Scharinger A, Eckrich S, Vandael DH, Schönig K, Koschak A, Hecker D, Kaur G, Lee A, Sah A, Bartsch D, Benedetti B, Lieb A, Schick B, Singewald N, Sinnegger-Brauns MJ, Carbone E, Engel J, Striessnig J (2015) Cell-type-specific tuning of Cav1.3 Ca(2+)-channels by a C-terminal automodulatory domain. Front Cell Neurosci 9:309. CrossRef Medline

Schnee ME, Ricci AJ (2003) Biophysical and pharmacological characterization of voltage-gated calcium currents in turtle auditory hair cells. J Physiol 549:697–717. CrossRef Medline

Schnee ME, Santos-Sacchi J, Castellano-Muñoz M, Kong JH, Ricci AJ (2011) Calcium-dependent synaptic vesicle trafficking underlies indefatigable release at the hair cell afferent fiber synapse. Neuron 70:326–338. CrossRef Medline

Seiler C, Nicolson T (1999) Defective calmodulin-dependent rapid apical endocytosis in zebrafish sensory hair cell mutants. J Neurobiol 41:424–434. Medline

Singh A, Gebhart M, Fritsch R, Sinnegger-Brauns MJ, Poggiani C, Hoda JC, Engel J, Romanin C, Striessnig J, Koschak A (2008) Modulation of voltage- and Ca2+-dependent gating of CaV1.3 L-type calcium channels by alternative splicing of a C-terminal regulatory domain. J Biol Chem 283:20733–20744. CrossRef Medline

Skinner LJ, Enée V, Beurg M, Jung HH, Ryan AF, Hafidi A, Aran JM, Dulon D (2003) Contribution of BK Ca^{2+}-activated K^+ channels to auditory neurotransmission in the Guinea pig cochlea. J Neurophysiol 90:320–332. CrossRef Medline

Spassova MA, Avissar M, Furman AC, Crumling MA, Saunders JC, Parsons TD (2004) Evidence that rapid vesicle replenishment of the synaptic ribbon mediates recovery from short-term adaptation at the hair cell afferent synapse. J Assoc Res Otolaryngol 5:376–390. CrossRef Medline

Striessnig J, Pinggera A, Kaur G, Bock G, Tuluc P (2014) L-type Ca channels in heart and brain. Wiley Interdiscip Rev Membr Transp Signal 3:15–38. CrossRef Medline

Tan BZ, Jiang F, Tan MY, Yu D, Huang H, Shen Y, Soong TW (2011) Functional characterization of alternative splicing in the C terminus of L-type CaV1.3 channels. J Biol Chem 286:42725–42735. CrossRef Medline

Vincent PF, Bouleau Y, Safieddine S, Petit C, Dulon D (2014) Exocytotic machineries of vestibular type I and cochlear ribbon synapses display similar intrinsic otoferlin-dependent Ca2+ sensitivity but a different coupling to Ca2+ channels. J Neurosci 34:10853–10869. CrossRef Medline

Westerman LA, Smith RL (1984) Rapid and short-term adaptation in auditory nerve responses. Hear Res 15:249–260.

Yang PS, Alseikhan BA, Hiel H, Grant L, Mori MX, Yang W, Fuchs PA, Yue DT (2006) Switching of Ca^{2+}-dependent inactivation of CaV1.3 channels by calcium binding proteins of auditory hair cells. J Neurosci 26:10677–10689. CrossRef Medline